LUND UNIVERSITY

Picosecond X-ray Diffraction Studies of Bulk and Nanostructure Materials

Jurgilaitis, Andrius

2012

Link to publication

Citation for published version (APA):
Jurgilaitis, A. (2012). *Picosecond X-ray Diffraction Studies of Bulk and Nanostructure Materials*. [Doctoral Thesis (compilation), Atomic Physics].

Total number of authors:
1

General rights
Unless other specific re-use rights are stated the following general rights apply:
Copyright and moral rights for the publications made accessible in the public portal are retained by the authors and/or other copyright owners and it is a condition of accessing publications that users recognise and abide by the legal requirements associated with these rights.
• Users may download and print one copy of any publication from the public portal for the purpose of private study or research.
• You may not further distribute the material or use it for any profit-making activity or commercial gain
• You may freely distribute the URL identifying the publication in the public portal

Read more about Creative commons licenses: https://creativecommons.org/licenses/

Take down policy
If you believe that this document breaches copyright please contact us providing details, and we will remove access to the work immediately and investigate your claim.

LUND UNIVERSITY

PO Box 117
221 00 Lund
+46 46-222 00 00

Picosecond X-ray Diffraction Studies of Bulk and Nanostructure Materials

Andrius Jurgilaitis

Lund 2012

Atomic Physics Division
Department of Physics
Lund Institute of Technology
Box 118, SE-221 00 LUND
SWEDEN

Lund Reports on Atomic Physics, ISSN 0281-2762
LRAP-448
ISBN 978-91-7473-225-2

© Andrius Jurgilaitis 2012
Printed in Sweden by *Media-Tryck*, Lund.
March 2012.

To my family ...

Sammanfattning

Snabba fenomen, som inträffar efter laserexcitation, har studerats med tidsupplöst röntgendiffraktion (TXRD). I de flesta experimenten har en ljuspuls från en femtosekundlaser använts för att excitera provet, och dynamiken har undersökts med röntgenljus. Tidsupplösta röntgendiffraktionsmätningar har utförts för att studera fasta halvledarmaterial, vätskor, ferro-elektrisk domänswitchning i kaliumdivätefosfat (KDP) och tryckvågsutbredning i grafit och halvledande nanotrådar.

När en laserpuls absorberas av ett fast material kan en mängd olika fasövergångar och andra fenomen induceras. Om laserpulsen innehåller tillräckligt mycket energi för att smälta materialet, kan repetitiv belysning skapa periodiska strukturer på provets yta. Denna effekt har studerats med statisk röntgendiffraktion, och har visat sig vara viktig då vätskespridningsexperiment utförs på repetitivt smälta prover. När energin i laserpulsen inte är tillräcklig för att inducera smältning kan koherenta fononer exciteras. Denna effekt har studerats i halvledande nanotrådar.

Tidsupplösningen för en synkrotronljuskälla bestäms av längden av en elektronpuls i lagringsringen, och är typiskt 50 - 300 ps. Bättre tidsupplösning kan uppnås genom att använda kortare röntgenpulser, som de som produceras vid Swiss Light Source (SLS), eller snabba detektorer, som t.ex. streak-kameran som används vid MAX-lab.

Röntgendiffraktion är en mycket känslig teknik för att studera strukturer, eftersom röntgenfotoner sprids från alla elektroner i provet. Spridd röntgenstrålning kan användas för att rekonstruera provets atomära struktur. I TXRD exciteras provet och belyses därefter med röntgenljus efter en given tidsfördröjning. Detta ger en ögonblicksbild av strukturen vid en tidpunkt. Flera bilder kan sammanställas för att skapa en film som visar de strukturella ändringarna i realtid. Detta har utförts med nanosekund-upplösning vid MAX-lab när en laser-genererad vätska studerades. Utvecklingen av en streak-kamera med tidsupplösning bättre än en pikosekund har varit en förutsättning för flera av studierna som presenteras i denna avhandling. Denna detektor har använts för att studera akustiska vibrationer i nanotrådar av indiumantimonid (InSb). Oscillationer med en period av 30-70 ps har detekterats, och har härletts till akustiska fononer i nanotråden. En dramatisk sänkning av ljudhastigheten har också observerats i dessa strukturer.

Abstract

Fast phenomena occurring after laser excitation were studied using time-resolved X-ray diffraction (TXRD). In most experiments, a femtosecond laser pulse was used to excite the sample, and X-rays were used as a probe. The X-ray diffraction technique was used to study bulk semiconductor samples, molten liquids, ferro-electric domain switching in potassium dihydrogen phosphate (KDP), and strain propagation in graphite and semiconductor nanowires. When a laser pulse is absorbed by a solid, a wide range of phase transitions and phenomena can be induced. If the laser fluence is high enough to melt the material, repetitive illumination will create periodic structures on the surface of the sample. This effect was studied using static X-ray diffraction, and it was shown that the effect is important if liquid scattering experiments are carried out on molten samples using the laser in repetitive mode. When the laser fluence is too low to cause sample melting, coherent acoustic phonons can be excited, and this effect was studied in semiconductor nanowires. The time resolution of the synchrotron light source is defined by the length of the electron bunch in the storage ring, and is typically 50-300 ps. In order to achieve higher time resolution, short X-ray pulses, such as those at the SLS, or fast detectors, such as the streak cameras available at MAX-lab can be used. X-ray diffraction is a very sensitive technique for the study of structures, since X-ray photons scatter from all the electrons in the sample. Scattered X-rays can be used to recreate the atomic structure in the sample. In TXRD the sample is perturbed and subsequently probed after a certain delay, giving a snapshot of the structure at a given time. Several images can be merged providing a real-time movie of the structural changes. This was achieved with nanosecond time resolution at MAX-lab, when a laser-created liquid was studied. The development of a sub-picosecond, hard X-ray streak camera was one of the prerequisites for many of the studies presented in this thesis. This detector was used to study the acoustic vibrations in InSb nanowires. Oscillations with a period of 30-70 ps were recorded, and were attributed to acoustic phonons in the semiconductor nanowire. A dramatic decrease in the velocity of acoustic waves was also observed in these structures.

List of publications

This thesis is based on the following papers and manuscripts.

I. R. Nüske, C. V. Korff Schmising, A. Jurgilaitis, H. Enquist, H. Navirian, P. Sondhauss, and J. Larsson, "Time-resolved x-ray scattering from laser-molten indium antimonide", *A REVIEW OF SCIENTIFIC INSTRUMENTS*, vol. 81, p. 013106, 2010.

II. A. Jurgilaitis, R. Nüske, H. Enquist,H. Navirian, P. Sondhauss, and J. Larsson, "X-ray diffraction from the ripple structures created by femtosecond laser pulses", *APPLIED PHYSICS A-MATERIALS SCIENCE & PROCESSING*, vol. 100, p. 105, 2010.

III. R. Nüske, A. Jurgilaitis, H. Enquist, S. D. Farahani, J. Gaudin, L. Guerin, M. Harb, C. V. Korff Schmising, M. Stormer, M. Wulff, and J. Larsson, "Picosecond time-resolved x-ray refectivity of a laser-heated amorphous carbon film", *APPLIED PHYSICS LETTERS*, vol. 98, p. 101909 , 2011.

IV. M. Harb, A. Jurgilaitis, H. Enquist, R. Nüske, C. V. Korff Schmising, J. Gaudin, S. L. Johnson, C. J. Milne, P. Beaud, E. Vorobeva, A. Caviezel, S. Mariager, G. Ingold, and J. Larsson, "Picosecond Dynamics of Laser-Induced Strains in Graphite", *PHYSICAL REVIEW B*, vol. 84, p. 045435 , 2011.

V. A. Jurgilaitis, M.Harb, H.Enquist, R. Nüske, A.I.H. Persson, M.Borg, K. Dick, H. Linke, L. E. Wernersson, and J. Larsson , "Studies of phonon propagation in InSb nanowires using time-resolved X-ray diffraction" , *In manuscript.*

VI. A. Jurgilaitis, M.Harb, H.Enquist, R. Nüske, M.Borg, K. Dick, H. Linke, L. E. Wernersson, and J. Larsson "Measurements of light absorption efficiency in InSb nanowires", *In manuscript.*

Papers not included in the thesis:

VII. H. Enquist, H. Navirian, R. Nüske, C. V. Korff Schmising, A. Jurgilaitis, M. Herzog, M. Bargheer, P. Sondhauss, J. Larsson, "Subpicosecond hard x-ray streak

camera using single-photon counting", *OPTICS LETTERS*, vol. 35, p. 3219, 2010.

VIII. H. Navirian, H. Enquist, R. Nüske, A. Jurgilaitis, C. V. Korff Schmising, P. Sondhauss, and J. Larsson, "Acoustically driven ferroelastic domain switching observed by time-resolved x-ray diffraction", *PHYSICAL REVIEW B*, vol. 81, p. 024113, 2010.

IX. J. Gaudin, B. Keitel, A. Jurgilaitis, R. Nüske, L. Guérin, J. Larsson, K. Mann, B. Schäfer, K. Tiedtke, A. Trapp, Th. Tschentscher, F. Yang, M. Wulff, H. Sinn, and B. Flöter, "Time-resolved investigation of nanometer scale deformations induced by a high flux x-ray beam" *OPTICS EXPRESS*, Vol. 19, p. 15516-15524, 2011.

X. R. Nüske, A. Jurgilaitis, H. Enquist, M. Harb, Y. Fang, U. Hakanson, J. Larsson, "Transforming graphite to nanoscale diamonds by a femtosecond laser pulse", *To appear in Applied Physics Letters*

Acknowledgements

The work presented in this thesis could not have been done without the support and collaboration of many people.

I would like to express my sincere gratitude to my supervisor, Professor Jörgen Larsson, for inviting me to join his research group, for placing his trust in me, for giving me the opportunity to work in the field of ultrafast science, and for guiding me through it.

I would also like to express many sincere thanks to Dr. Peter Sondhauss, for our constant discussions, and for his support, suggestions and belief in me. You are a great teacher and I have learned a great deal from you.

Many thanks to my colleagues: Henrik Enquist, Maher Harb, Ralf Nüske, Hengameh Navirian, Clemens v. Korff Schmising and Anna Persson, for all their help, discussions and for creating a pleasant working environment. Many thanks to Henrik, the timing guru. Thanks for all the tricks you showed me. I am grateful to Maher for showing me many Matlab tricks, for useful discussions and for experimental help in the lab. Thanks to Ralf for being supportive in the courses and experiments, and for all our interesting discussions at the lab.

I would like to thank Gvidas Astromskas for giving me access to the scanning electron microscope and other nanoworld devices. I enjoyed the time spent in the cleanroom lab very much. Thanks to Mattias Borg for interesting discussions on nanowires and the samples you made for me.

Many thanks to the administrative and technical staff at MAX-lab and at the Division of Atomic Physics; especially Minna Ramkull, Camilla Nilsson, Lisa Dahlström, Anders Månsson, and others, for giving me their help and support when I needed it most.

Many, many thanks to my family, especially my wife, Vilma, for her boundless optimism and love, and for being supportive during my PhD studies.

Thanks to my parents for their constant trust in me, and for being supportive

during the dark times.

Thanks to the members of IFLKK, for being with me and my family during this period. Thanks to Anders, Mattias, Markus, Natali, Helen, Simon, Daniel, Tony, Tay, Ulf, Peter, Martin, Nadia, Matilda, and everyone else. It was a pleasure to meet you, and you enriched my social life.

I am grateful to the MAXLAS network allowing me to work in X-ray science and the field of laser physics.

My heartfelt thanks to everyone who directly or indirectly contributed to this work.

Contents

Part I

Overview

Chapter 1

Introduction

The best known method of studying the structure of condensed matter on the atomic scale is X-ray diffraction. It is mainly used to analyse crystalline structures such as semiconductors [1] and metals [2], but it can also be applied to improve our understanding of nanomaterials such as nanowires [3]. Diffraction is observed when electromagnetic radiation interacts with structures that have a geometric size comparable to the wavelength of the radiation. Since the wavelength of X-rays is comparable to the interatomic distances in crystals and molecules, X-ray diffraction patterns can be used to accurately determine atomic positions.

Time-resolved X-ray diffraction (TXRD) is a relatively new technique, allowing atomic and molecular dynamics to be visualized [4], [5]. This method combines ultrafast lasers and X-ray diffraction, where the laser is used to excite the sample and X-rays are used as a probe. In order to follow the fast dynamics initiated by the laser, short X-ray pulses or fast detectors such as a streak camera must be used. The time resolution is determined by the duration of the X-ray pulse or the response of the detector. The pulse duration of a typical X-ray bunch from a synchrotron radiation source is a few hundreds of picoseconds, while fast detectors can provide sub-picosecond time resolution. The constant development of X-ray sources is opening up new opportunities. Nowadays, there are X-ray sources that can produce pulses shorter than 100 fs. Examples are free-electron lasers (FELs), X-ray slicing sources at synchrotrons and laser-based X-ray sources.

The work presented in this thesis is mainly based on time-resolved X-ray scattering techniques, which were used to probe the structural dynamics in materials. The time scale studied ranges from below a picosecond to several microseconds.
This thesis is organized as follows. Chapter 2 reviews the general formalism of X-ray diffraction. Static and time-resolved X-ray scattering from solids and liquids is discussed. Chapter 3 describes the materials that were investigated, and the scientific motivation for the studies is discussed. In Chapter 4, the sample excitation mechanisms are described, including the creation and detection of coherent acoustic phonons in bulk semiconductors and nanowire samples. Chapter 5 describes beamline D611

at MAX-lab, where most of the experiments were carried out. The X-ray source, the laser system and the fast detector are discussed in detail. Chapter 6 provides general information on the experiments performed. The experimental set-up and geometry are briefly explained. Finally, Chapter 7 provides an outlook on future work.

Chapter 2

Description of X-ray Methods

2.1 X-ray scattering

Electromagnetic waves (X-rays) and condensed matter interact in two ways: by elastic and inelastic scattering. In the case of elastic scattering the X-ray energy is unchanged, while inelastic scattering results in a decrease in the X-ray photon energy. Incoming X-rays can "kick out" electrons from their bound states in a process called photoionization. In this process, momentum and energy are transferred from the incoming photon to excite the electron. Another inelastic scattering process is Compton scattering, where part of the photon energy is transferred as kinetic energy to an electron and the decreased photon energy results in a red shift. Inelastic scattering can often be neglected, since scattered waves have different energies and will not add coherently. At low energies the dominant scattering mechanism is Thomson scattering, during which the X-rays are elastically scattered by electrons. This can be envisioned by considering that electrons that are subjected to an electromagnetic wave start to oscillate at the frequency of the incoming electromagnetic wave and become a source of dipole radiation. In this case the photon energy is conserved. The wavelength of the emitted radiation will be the same as that of the incoming wave, but the phase will be shifted by 180 degrees. Since this phase shift occurs for every scattered wave it will not influence the scattering intensity pattern from a given electron distribution.
The scattering of X-rays by a single electron is illustrated in Fig. 2.1.
The intensity of the scattered radiation at a distance

$$I(R) = I_0 \frac{r_e^2}{R^2} P \tag{2.1}$$

where $r_e = e^2/(4\pi\epsilon_0 mc^2)$ is the classical electron radius, R is the distance from the scattering centre, P is the polarization factor.

When X-rays interact with a number of electrons the scattered waves interfere. Scattering from the atom can be visualized if one assumes that the scattered X-rays

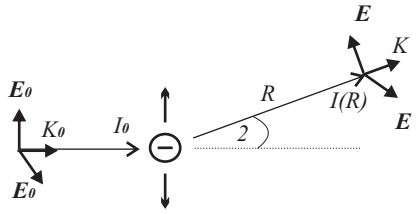

Figure 2.1: Scattering of X-rays by a single electron.

originate from an electron cloud with a charge density $\rho(\vec{r})$ The total scattering is then calculated by summing over the whole atom (electron cloud), taking phase differences into account:

$$f(\vec{Q}) = \int \rho(\vec{r}) exp(i\vec{Q}\vec{r}) d\vec{r} \tag{2.2}$$

where $f(\vec{Q})$ is called atomic scattering factor or form factor, $\vec{r}$ is the position vector, $\vec{Q}$ is the scattering vector.
The scattering vector is defined as $\vec{Q} = \vec{k} - \vec{k_0}$, where $\vec{k_0}$ and $\vec{k}$ are the incoming and scattered wave vectors, respectively, and $|k| = 2\pi/\lambda$. In the case when $\vec{Q} = 0$, integration need only be performed for the charge distribution. In this case, the integral is equal to the number of electrons in the atom, Z. If $\vec{Q} > 0$, the form factor has to be calculated as a function of $\vec{Q}$. The form factor $f(\vec{Q})$ converges towards zero for large $\vec{Q}$, $f(\vec{Q} \Rightarrow \infty) = 0$, since different volume elements scatter out of phase.

X-ray scattering from single atoms has been calculated for all chemical elements using various quantum mechanical methods, and can be parameterized using the following expression:

$$f = \sum_{j=1}^{4} a_j exp(-b_j sin^2\theta/\lambda^2) + c \tag{2.3}$$

where the coefficients a_j, b_j and c can be found in International Tables for Crystallography [6].
If the atoms are arranged and form a molecule the scattering consists of atomic contributions and can be expressed by the structure factor:

$$F^{mol}(\vec{Q}) = \sum_{\vec{r_j}} f_j(\vec{Q}) exp(i\vec{Q}\vec{r_j}) \tag{2.4}$$

where $\vec{r_j}$ is the position vector of the atom in the molecule.

The intensity of scattering scales with the square of the structure factor. Hence, in a diffraction experiment where the intensity is recorded, the phase information is

lost. In order to determine the intensity of the X-rays scattered from a crystal, one can decompose the crystal into a lattice and a basis. A basis can consist of more than one atom. A copy of the basis is placed at each lattice point see (Fig. 2.2).

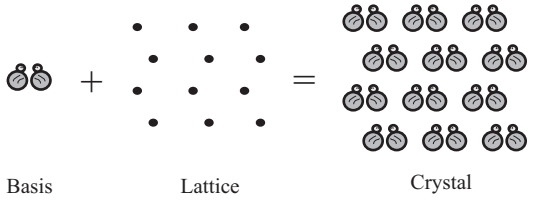

Figure 2.2: Schematic representation of the crystal.

The lattice is a mathematical construction of points that reflects the translational symmetry of the crystal. The basis gives the atomic position within the unit cell defined by the lattice. If $\vec{R}_n$ denotes the lattice vectors defining the lattice, and $\vec{r}_j$ the positions of the atoms in the unit cell, the scattering from the crystal can be written:

$$F^{crystal}(\vec{Q}) = \overbrace{\sum_{\vec{r}_j} F_j^{mol}(\vec{Q}) exp(i\vec{Q}\vec{r_j})}^{structure\ factor} \overbrace{\sum_{\vec{R}_n} exp(i\vec{Q}\vec{R}_n)}^{lattice\ sum} \tag{2.5}$$

The expression above can be understood as an integral over the electron density of all atoms $f_j(\vec{Q})$. It can be divided into a sum over the atoms in a unit cell (structure factor), and a sum over all lattice vectors (lattice sum). Scattering is strong when the terms $exp(i\vec{Q}\vec{R_n})$ add up in phase. Hence the maximum intensity will be observed if:

$$\vec{R_n} \cdot \vec{Q} = 2m\pi \tag{2.6}$$

where m is the reflection order.

The lattice vectors $\vec{R}_n$ are defined as:

$$\vec{R_n} = n_1\vec{a_1} + n_2\vec{a_2} + n_3\vec{a_3} \tag{2.7}$$

where n_1, n_2, n_3 are integers and $\vec{a_1}$, $\vec{a_2}$, $\vec{a_3}$ are basis vectors of the lattice. A solution to a Eq. 2.6 can be found if one introduces reciprocal lattice basis vectors $\vec{b_1}$, $\vec{b_2}$, $\vec{b_3}$ so that reciprocal lattice vector $\vec{G}$ is:

$$\vec{G} = h\vec{b_1} + k\vec{b_2} + l\vec{b_3} \tag{2.8}$$

where h, k, l are integers and

$$\vec{b_1} = 2\pi\frac{\vec{a_2} \times \vec{a_3}}{\vec{a_1} \cdot (\vec{a_2} \times \vec{a_3})},\ \vec{b_2} = 2\pi\frac{\vec{a_3} \times \vec{a_1}}{\vec{a_1} \cdot (\vec{a_2} \times \vec{a_3})},\ \vec{b_3} = 2\pi\frac{\vec{a_1} \times \vec{a_2}}{\vec{a_1} \cdot (\vec{a_2} \times \vec{a_3})} \tag{2.9}$$

Calculating the direct product of the reciprocal lattice vector $\vec{G}$ and the direct lattice vector $\vec{R_n}$ gives:

$$\vec{G} \cdot \vec{R_n} = 2\pi(hn_1 + kn_2 + ln_3) = 2\pi \times m \tag{2.10}$$

where m is an integer. From Eq. (2.10) it can be seen that the scattering amplitude from the crystal is maximal if the scattering vector coincidences with a reciprocal lattice vector:

$$\vec{Q} = \vec{G} \tag{2.11}$$

In a crystal, atoms are arranged periodically in planes separated by a distance called the interplanar distance. If the incoming X-rays enter the crystal at a specific angle to the surface, constructive interference from two lattice points A and D in adjacent planes can be written as $\overline{BD} + \overline{DC} = dsin\theta + dsin\theta$, see Fig. 2.3. This is Bragg's law:

$$\lambda = 2dsin\theta \tag{2.12}$$

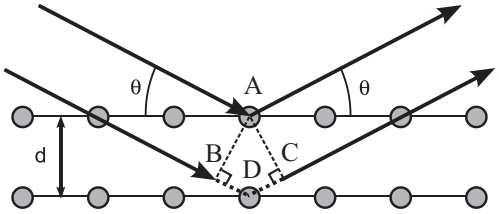

Figure 2.3: Diffraction from a crystal.

where θ is the angle of the wave vectors of the incident and reflected waves with respect to the diffracting lattice planes, d is the interplanar distance and n is an integer that denotes the reflection order. Constructive interference can only be achieved when the phase shift is a multiple of λ. Using Bragg's law one can find the position of the scattered X-rays in space.

2.2 X - ray scattering from solids and liquids

In order to describe X-ray scattering from perfect crystals, where multiple X-ray scattering and absorption cannot be neglected, dynamical diffraction theory must be used. Dynamical diffraction theory was used in the present work to model experimental results quantitatively (Paper II) [7]. The aspects of dynamical diffraction theory

that are important for this thesis are highlighted below. The details of dynamical diffraction theory can be found elsewhere [8], [9].

An incident beam becomes attenuated in a crystal, as shown schematically in Fig. 2.4. Attenuation is due to two phenomena: absorption and extinction. X-ray absorption is due to photoionization, and different materials have different X-ray absorption lengths [10], [11]. Extinction is due to elastic scattering, and is described by the dynamical theory of diffraction.

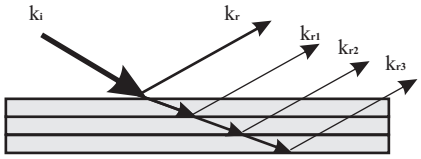

Figure 2.4: X-ray scattering from a perfect crystal.

The principle of the dynamical theory of X-ray diffraction is explained here, based on Darwin's model, where X-ray scattering from each atomic plane is taken into account [9]. Both the transmitted and the scattered waves shown in Fig. 2.4 must be taken into consideration. The transmitted beam is attenuated by both absorption and extinction. The depth at which the intensity is reduced by 1/e is called the attenuation depth, and this is a measure of how deep the beam propagates into the material. By making sure the X-rays enter at a grazing angle, it is possible to control the attenuation depth and hence the probe depth. The probe depth must match the laser pump depth when using a laser pump/X-ray probe technique. For low-Z materials the attenuation depth could be a few tens of micrometres, while the laser pump depth can be of the order of a hundred nanometres or less. Asymmetric reflection is a simple means of reducing the penetration depth, and hence probing the crystal only near the surface. In semiconductors, optical photons typically penetrate very little (of the order of nm) [12] while X-rays typically more than a micrometer [11]. Therefore, the sample-X-ray geometry must be carefully considered.

The reflectivity curve describes the ratio of the absolute square of the amplitudes of the incoming and reflected waves, as a function of the energy (or wavelength). The bandwidth: $\Delta E/E = \Delta\lambda/\lambda$, i.e. the width of the reflectivity curve, can be expressed using the differential form of Bragg's law:

$$\Delta\lambda/\lambda = \Delta\theta/tan\theta \quad and \quad \omega_{Darwin}^{FWHM} = \frac{3}{2\sqrt{2}}\, tan\,\theta\, \xi_{Darwin}^{total} \tag{2.13}$$

where $\xi_{Darwin}^{total} = 4/\pi(d/m)^2 r_e\,|F|\,/v_c$, d is the thickness, m is an integer (the order of the reflection), v_c is the volume of the unit cell and, F is the structure factor. The width of the reflectivity curve depends on various factors, such as the X-ray energy, Bragg angle, structure factor and asymmetry angle. Reflectivity curves are asymmetric and the reflectivity is always less than 1 due to absorption (see Fig. 2.5).

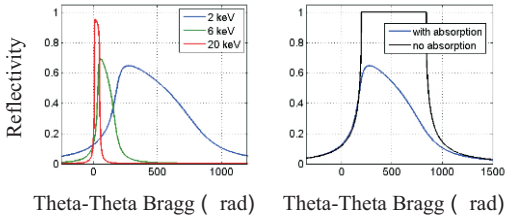

Figure 2.5: InSb 111 reflectivity curve at different photon energies. The reflectivity from InSb was calculated in connection with the work described in Paper II.

The diffraction geometry is referred to as symmetric if the sample surface is parallel to the diffracting planes, otherwise it is asymmetric. The asymmetry ratio is defined: $\gamma = cos(\psi_h)/cos(\psi_0)$, where ψ_h is the angle between the normal to the crystal surface and the reflected direction, and ψ_0 is the angle between the normal to the crystal surface and the incident direction. Fig. 2.6 shows three diffraction geometries. Different X-ray diffraction geometries result in different shapes, amplitudes and positions of the reflectivity curve. The asymmetric shape of the reflectivity curves arises from X-ray absorption, while the width of the rocking curves is dependent on the X-ray penetration depth. Another characteristic effect is the shift of the reflectivity curve, which can be explained by refraction. The diffraction peak moves towards higher angles for higher asymmetry ratios.

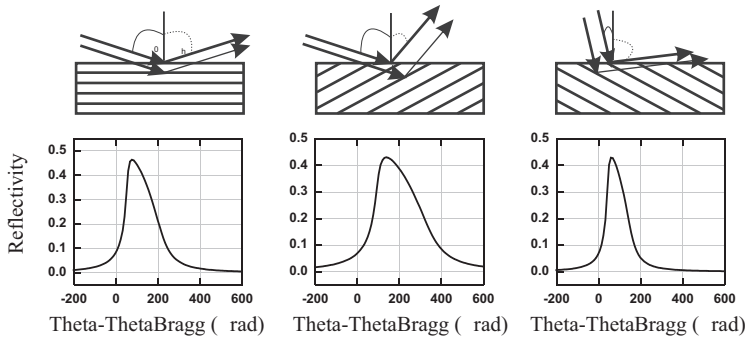

Figure 2.6: Symmetric and asymmetric reflections from the 111 plane of an InSb crystal.

Lattice vibrations (Debye-Waller factor)

Atoms are not stationary, but oscillate around their average position. The intensity of the scattered X-rays can be written [13]:

$$I = \sum_m \sum_n f(\vec{Q}) e^{-\frac{1}{2}Q^2\langle u_{Qm}^2\rangle} e^{i\vec{Q}\cdot\vec{R_m}} f^*(\vec{Q}) e^{-\frac{1}{2}Q^2\langle u_{Qn}^2\rangle} e^{i\vec{Q}\cdot\vec{R_n}} + \sum_m \sum_n f(\vec{Q}) e^{i\vec{Q}\cdot\vec{R_m}} f^*(\vec{Q}) e^{-i\vec{Q}\cdot\vec{R_n}} \left\{ e^{Q^2\langle u_{Qm} u_{Qn}\rangle} - 1 \right\} \quad (2.14)$$

where $\vec{R_n}$ is the time-averaged mean position in the unit cell, $\vec{u_n}$ is the displacement and, $\vec{Q}$ is the scattering vector. The first term in Eq. 2.14 corresponds to elastic scattering from the lattice with a reduced atomic form factor:

$$f^{atom} = f(\vec{Q}) e^{-\frac{1}{2}Q^2\langle u_Q^2\rangle} \equiv f(\vec{Q}) exp(-M) \quad (2.15)$$

where the exponential term is called the Debye-Waller factor. Thermal diffuse scattering is background between the Bragg peaks, which gives information about the phonon population. As the temperature increases, the average displacement increases, resulting in a decrease in the intensity in the elastic Bragg peak, but its width remains unchanged.

X-ray scattering from liquids

X-ray scattering techniques can also be applied to non-crystalline forms of matter such as liquids, rubber-like materials and gases. The structure of liquids is very different from that of crystals and hence the X-ray diffraction pattern is different. This is because there is no long-range order in liquids as the atoms are constantly in motion. However, there is some short-range order due to next-neighbour interactions, resulting in broad diffraction rings, as can be seen in Fig. 2.7.

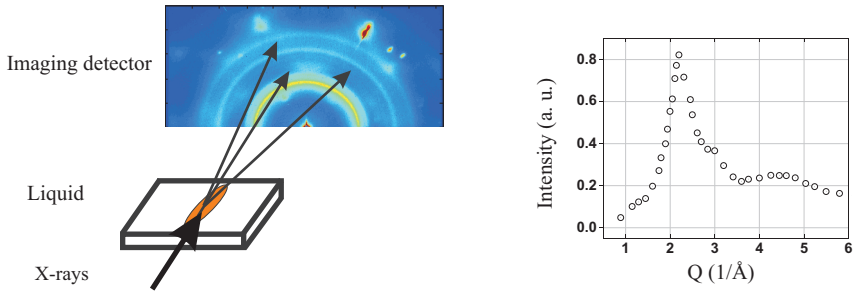

Figure 2.7: Schematic representation of X-ray scattering from a liquid (left), and a typical graph of the intensity of scattered X-rays as a function of the scattering vector (right).

The intensity distribution of scattered X-rays over the reciprocal space is described by the Debye scattering equation [8]:

$$I(Q) = \sum_m \sum_n f_m f_n \frac{sin(Qr_{mn})}{Qr_{mn}} \tag{2.16}$$

where $Q = 4\pi sin\theta/\lambda$, r_{mn} is the distance between atoms m and n, f is the atomic scattering factor. The equation above can be applied to any material that has only short-range order. The experimentally observed scattered X-ray intensity is expressed in arbitrary units, and must be normalized in order to calculate the radial distribution function. The radial distribution function can reveal information about nearest neighbour distances and coordination numbers (the number of nearest neighbours). The way in which the radial distribution function is calculated can be found in the literature [8].

2.3 Time-resolved X-ray diffraction

Many atomic processes take place on very short time scales (picoseconds or femtoseconds). Examples of such processes are chemical reactions [14], [15], the relaxation of excited electrons [16], [17], and non-thermal melting [18], [19], [20], [5]. The time scale is very short for a fundamental reason. For instance, a typical fast chemical reaction takes place on the femtosecond time scale because the typical length scale is of the order of an angstrom (i.e. the bond length [21]) and the atomic velocity is comparable to the speed of sound.

So-called pump/probe techniques can be used to resolve fast phenomena if short pulses are available. Present day technology can deliver both short laser pulses and short X-ray pulses [22]. A short laser pulse initiates a structural change, which manifests itself in a change in the scattered X-ray intensity, which is measured as a function of time. The time resolution is determined by the pulse duration and jitter. Several combinations of pump and probe can be used, depending on the aims of the experiment. The most common ones are: laser pump/probe, laser pump/X-ray probe or X-ray pump/probe [22], and X-ray pump/laser probe [23]. Monochromatic or broadband X-ray radiation can be used, depending on the kind of phenomenon to be studied. A visible pump together with an X-ray diffraction probe is the most direct technique for observing structural dynamics in matter. Light excitation induces variations in the intensity of the Bragg reflections and changes in peak position. The peak shifts are related to changes in the lattice constants. Laser illumination usually warms the sample, resulting in rapid heat expansion, which in term triggers acoustic waves. Acoustic waves induce changes in lattice spacing that can be studied with X-rays. Another interesting field in which optical pump/X-ray probe techniques have proven to be useful is the study of the ultrafast solid to liquid phase transitions that occur at the surface of a semiconductor when irradiated by a high-fluence laser pulse. Typically, a layer of a few tens of nanometres will melt in a few hundred femtoseconds [24].

2.4 Time-resolved specular X-ray reflectivity

A phenomenon known as total external reflection can be observed when X-rays are incident at small angles on a sample surface. This is because the refractive index is less than 1 for X-rays and can be written [13]:

$$n = 1 - \delta + i\beta \tag{2.17}$$

and

$$\delta = \frac{2\pi\rho r_e f(\vec{Q})}{k^2} \tag{2.18}$$

where

$$\beta = \frac{\mu}{2k} \tag{2.19}$$

where δ is the decrease in the refractive index, β is the absorption index, k is the wave vector, ρ is the electron density, r_e is the classical electron radius and μ is the absorption coefficient.
Thus, if the angle between the incoming X-rays and the surface is smaller than a critical angle total external reflection occurs. This critical angle, α_c, is defined as:

$$\alpha_c = \sqrt{2\delta} \tag{2.20}$$

This phenomenon can be used, for example, to study surface roughness, thin films and their properties [25]. Information on layer thickness, density and roughness can be extracted from the experimental data using a fitting procedure [26]. This technique was successfully applied in time-resolved studies, using a laser pump/X-ray probe technique (Paper III). Fig. 2.8 shows the simulated specular reflectivity for different configurations.

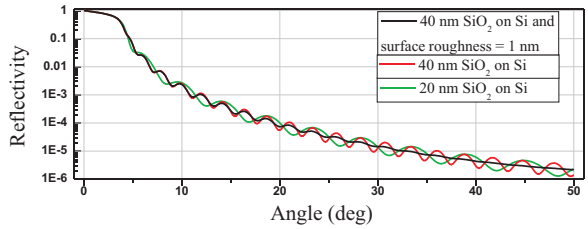

Figure 2.8: Simulated variation in X-ray intensity as a function of the angle between the X-rays and the sample surface. The effect of layer thickness and surface roughness can be clearly observed.

The oscillatory part derives from the constructive interference between the waves reflected from the vacuum/SiO2 and SiO2/Si interfaces. The period gives the thickness of the layer. The laser-introduced surface roughness has an impact on the contrast of the interference fringes.

Chapter 3

Materials Investigated

A number of different materials were investigated in the work presented in this thesis. In the following sections the properties of bulk InSb, InSb nanowires, natural graphite and amorphous graphite are summarized. The characteristics of the materials and sample preparation are described briefly.

3.1 InSb crystals: bulk and nanostructures

Indium antimonide (InSb) is a narrow-band-gap (0.17 eV at 300 K) Group III-V semiconductor material with elements of high atomic numbers. It can be used in fast electronics and infrared detectors, due to its small effective electron mass and small band gap, allowing for electron-hole pair generation using photons with energies corresponding to wavelengths of 1-5 μm. It is also a promising material for thermoelectric applications [27].

Developments in the semiconductor industry raise new problems and new ways of solving them. For instance, making artificial semiconductor structures such as nanowires could in principle provide the solution to many problems [3]. Nowadays, these structures can be made using chemical beam epitaxy or metal organic vapour phase epitaxy (MOVPE). It has been found that semiconductor nanowires are a better choice than bulk material for thermoelectric applications [28], [29]. This is because the heat transport in nanowires is slower than in bulk materials, due to the domination of different phonon scattering mechanisms. The large surface-to-volume ratio of nanowires gives them an advantage in photonics, e.g. in solar cells or LEDs [30], [31]. Although substantial efforts have been, and are being, made to characterize nanowires, it is still not possible to verify some of their predicted properties. Some of the difficulties in investigating these materials lie in the fact that the technology is advanced and nanowires are difficult to grow. A better understanding of the underlying physics of nanowires could be achieved by carrying out structural dynamic studies using TXRD. Pump/probe experiments on nanostructures are difficult since the excitation mechanisms with visible radiation are not well known. X-ray probing can be problematic

due to poor X-ray reflectivity and the risk of inducing permanent radiation damage. The advent of new intense powerful X-ray sources such as SLAC National Accelerator Laboratory, USA, MAX IV in Sweden and The European X-ray Laser Project XFEL in Germany, may help to overcome these problems.

Bulk InSb

Most bulk III-V semiconductor materials have a zinc blende (ZB) crystal structure (FCC), and InSb is no exception. It consists of two heavy elements with Z = 49 (In) and 51 (Sb). They are bound to each other by covalent sp3 bonds that are oriented tetrahedrally (see Fig. 3.1). InSb is a very popular material for TXRD experiments due to its high scattering power.

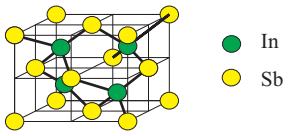

Figure 3.1: The zinc blende crystal structure of bulk InSb.

InSb nanowires

Bulk and nanowire InSb both have a zincblende crystalline structure, whereas other III/V nanowires may have a ZB structure, a wurtzite (WZ) structure, or a mixture of both. The WZ structure consists of two hexagonal close packed lattices (see Fig. 3.2). In both cases, the atoms are tetrahedrally bound to their neighbours, but the two different structures have different properties. For instance, the band gap is larger in WZ. The crystal structure of the nanowire can be controlled to some extent by the growth conditions [32].

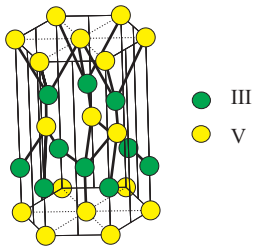

Figure 3.2: The wurtzite crystal structure of an InSb nanowire.

The difference in atoms and their electronegativity "modifies" the covalent bonds introducing an ionic component called the a.k.a. ionicity [33]. The ionicity determines whether the material is WZ or ZB; higher ionicity favouring the stable WZ crystal structure [34], [35].

3.2 InSb nanowires: growth, characterization and properties

The samples used for experimental studies in this thesis were grown using MOVPE [36]. In order to grow nanowires, a catalyst or seed particle is required for each wire, usually gold (Au). The size of the seed particle determines the diameter of the wire, while the length of the wire depends strongly on the growth conditions (temperature, time, etc.). The gold particles are first deposited on the substrate (e.g. InAs), after which the sample is placed in a reactor. The gold-assisted nanowire growth mechanism can be explained using the vapour-liquid-solid model [37], [38]. The seed particle acts as a collector that attracts the material (Group III) from the vapour. Nanowire growth starts under the seed particle, where supersaturation is reached and where crystallization of the material starts. The growth of the nanowire is based on the fact that the material precipitates to the liquid/solid interface. In this way, the system goes from a state of high to low chemical potential. Since the Au/substrate interface is the only place where supersaturation is reached, the precipitated Group III material combines with the Group V material from the gas phase to form a crystal. The nanowires grow perpendicular to the surface of the substrate. If the growth conditions are correct the fastest growth is under the seed particle, thus, the facets of the wire and the substrate grow very little. A schematic illustration of nanowire growth is shown in Fig. 3.3

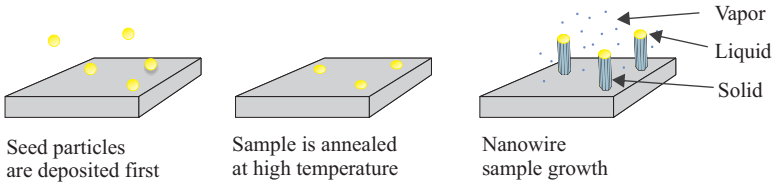

Figure 3.3: Schematic illustration of how nanowires are grown.

Sample characterization

It is not possible to obtain complete information on the quality of the samples using an optical microscope (OM), as the resolution is limited by the wavelength of light, as can be expressed using the Abbe equation:

$$d = \frac{0.612\lambda}{nsin\theta} \tag{3.1}$$

where λ is the wavelength, n is the refractive index and θ is the aperture angle.

Since the length of the nanowires is of the order of a micrometre the OM can give some information about its structure. However, a more detailed picture is usually required and, therefore, a scanning electron microscope (SEM) is often used. The de

Broglie wavelength of electrons is very small and depends on the accelerating voltage of the microscope, and a resolution better than 1 nm can be achieved. When the electron beam interacts with the sample a number of different "signals" are produced. These are detected and converted into an electronic signal. Fig 3.4 illustrates the interaction of the electron beam with a sample and shows a typical SEM image of nanowires.

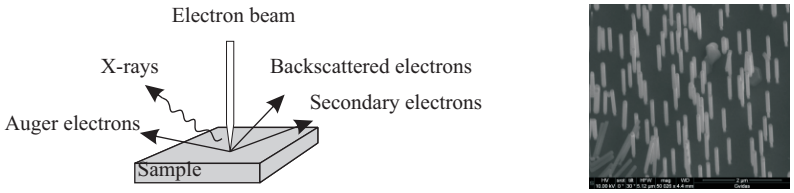

Figure 3.4: Interaction of the electron beam with a sample generates a number of different signals (left). A typical SEM image (right).

Another tool that can be used to study nanometre-sized objects is the atomic force microscope (AFM). An AFM can be used to study nano-scale structures on both conducting and insulating surfaces. In this work, an AFM was used to visualize the morphology of a laser-irradiated InSb surface. The data were used to simulate X-ray reflectivity curves (Paper II). Fig 3.5 shows a sketch of an AFM and a typical AFM image.

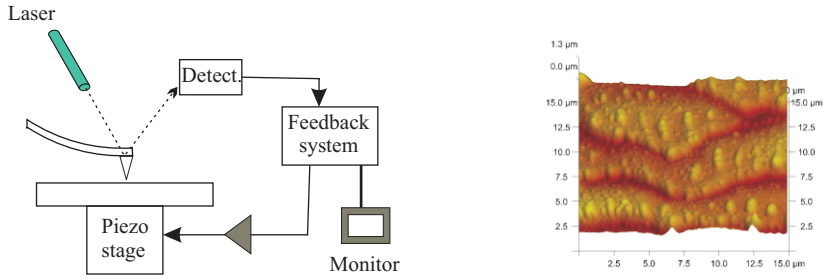

Figure 3.5: The working principle of an AFM (left) and a typical image from AFM measurements (right).

Heat transport in nanowires and thermoelectrics

The studies presented below focused on thermal transport in nanowires. It has been shown theoretically and experimentally that heat transfer in silicon nanowires is slower than in bulk material [38]. The suitability of a material for thermoelectric applications can be described by the thermoelectric figure of merit, denoted ZT: the higher the

value, the better the thermoelectric device that can be made:

$$ZT = S^2\sigma T/\kappa \tag{3.2}$$

where S is the thermoelectric power, σ is the electrical conductivity, κ is the thermal conductivity, T is the absolute temperature (operating temperature of the device).

An ideal thermoelectric material is one that scatters phonons efficiently while electronic transport is not affected [39]. It is difficult to increase ZT for bulk materials due to the Wiedemann-Franz law, which relates the electric and thermal conductivities: $\kappa/\sigma = LT$, where L is the Lorenz number ($2.44x10^{-8}\ W\Omega/K^2$). In nanostructures (quantum well superlattices and nanowires) there is the potential to increase ZT [40]. Semiconductors such as InSb are interesting since the thermal conductivity can be separated into two parts, the electronic part and the phononic part ($\kappa = \kappa_{electron} + \kappa_{phonon}$), where the electronic contribution is smaller than the phononic. The confined electrons are able to move freely (at least in one direction), while phonon scattering is increased due to the surfaces of the wire. As a result, the thermal conductivity of the lattice is reduced and ZT is increased. A reduction in the speed of sound reduces the thermal $\kappa = 1/3(Clv)$, where C is the specific heat, l is the mean free path of the phonons and v is the velocity of sound [41]. This can be achieved, using materials with high atomic numbers. The electronic heat conductivity can be neglected and only the phononic conductivity need be considered. Nanostructures could be produced in such a way that the dimensions are smaller than the mean free path of the phonons, and at the same time larger than that of electrons and holes. The phonons, which are mainly responsible for heat transfer, experience increased scattering from the surfaces. This indicates that the thinner the wire, the larger the surface area per unit volume, thus the greater the scattering, and the smaller the thermal conductivity. At the same time, electrons can move freely along the wire and the electrical properties should be similar to those of the bulk material. It has been found that thermal conductivity is strongly dependent on diameter. The conventional method of measuring thermal conductivity is challenging with respect to sample preparation [29]. Since the speed of sound is directly related to thermal conductivity [42], an alternative method is to measure the speed of sound, e.g. using TXRD [42], [43]. The advantage of this method is that sample preparation is less complex, and the measurements can be conducted on the ensemble of wires on the substrate. Such experiments were included in this work and are described in Paper V and Paper VI.

3.3 Carbon-based materials: natural crystalline graphite and amorphous graphite

Carbon-based materials come in many forms due to the ability of carbon to form different types of bonds. Laser-excited carbon material can undergo a structural change, which has been shown experimentally and proven theoretically [44], [45]. Carbon-based materials find applications in many areas [46], [47], and, therefore, a

more detailed understanding of its nature is needed. A number of carbon samples have been studied in the present work using the pump/probe technique. Amorphous carbon is made using standard film deposition and growth techniques (for instance, chemical vapour deposition). It exhibits only short-range order and has many dangling bonds. Its properties depend on the growth parameters. Paper III describes how the time-resolved X-ray specular reflectivity technique can be used to record small changes in the X-ray scattering signal on very fast time scales. Crystalline graphite is the form of carbon that is found naturally. It has a hexagonal layered structure in which graphene sheets are stacked in the order AB and shifted slightly with respect to each other (see Fig. 3.6).

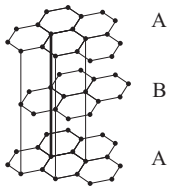

Figure 3.6: Structure of natural crystalline graphite.

The graphene layers are bound to each other by weak van der Waals forces, while the in-plane bonds are strong covalent bonds. Each carbon atom has three in-plane neighbours. Carbon has four valence electrons; three of which are used to make strong covalent bonds with their neighbours in the plane, while the fourth electron is "free" and can travel along the sheet. Because of its layered structure graphite is very anisotropic. For instance, it is a good thermal insulator along the c-axis perpendicular to the graphene sheets, while in-plane heat is transported very quickly. Graphene layers can be removed from a graphite crystal using laser ablation. The precursor to this is a large strain wave propagating into the material. Laser-induced strain waves propagating in natural graphite have been investigated and are discussed in Paper IV.

Chapter 4

Material Excitation and Relaxation Mechanisms

There are many ways to excite the sample for pump/probe studies. The most common is light excitation using a laser. In this chapter, the processes that take place in the sample after laser excitation are described.

4.1 Phonons and the dispersion relation

Atomic vibrations in solids are quantized into phonons, the energy of which is determined by the vibrational frequency. The frequency ω and the wave number k are related via the dispersion relation. The number of branches in the dispersion relation is related to the number of atoms in the unit cell. Three branches originate from acoustic phonons (one longitudinal and two transversal modes) and have zero frequency at k = 0, while the remaining branches with non-zero frequency arise from optical phonons. The number of optical branches is 3N-3, where N is the number of atoms in the unit cell. The number of branches can vary significantly in very thin wires, where quantum effects influence the phonon dispersion relation [48], [49].

4.2 The interaction of light with solids

A wide range of processes is initiated when light is absorbed in a solid material such as a semiconductor. If the intensity of the incoming light is low, the energy deposited only increases the temperature near the surface of the sample, and the morphology of the surface is unchanged. If the intensity of the incoming light is very strong it may melt the sample, causing permanent damage, and ripple-like structures can be observed (Paper II). When the incoming light reaches the sample surface, part of it is reflected and the other part is transmitted into the sample. The splitting of the light at an interface can be calculated using Fresnel's equations [50]. The electromagnetic waves (light) are able to exchange energy with matter only in quanta

$\hbar\omega$. In a semiconductor at absolute zero (0 K) the valence band is completely filled and the conduction band is empty (see Fig. 4.1). In this case, absorption takes place only when the energy of the photon is greater than the band gap. When the electron is excited to the conduction band a hole is created in the valence band.

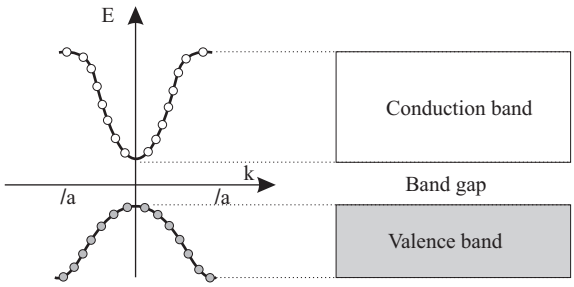

Figure 4.1: Semiconductor band structure.

It should be noted that the optical parameters of the material depend strongly on the intensity of the incoming light. At high intensity a number of nonlinear effects can be observed, such as multiphoton absorption, free carrier absorption and the so-called Burstein-Moss shift. The Burstein-Moss shift means that the absorption edge is blue shifted due to the population of electron states close to the bottom of the conduction band. Briefly, after laser irradiation, the carriers are not in thermal equilibrium with the lattice. Depending on the excitation power and the material, the temperature of the carriers is usually higher than the lattice temperature, and excess energy is released through scattering processes.

4.3 Relaxation mechanisms

The absorbed photon can create an electron-hole pair or excite a free carrier. In semiconductors where the incident optical photons have energies larger than the band gap, interband absorption is usually dominant. Energy is released via carrier-carrier collisions and the emission of phonons [51]. Free carrier absorption and multiphoton absorption can usually be neglected. This kind of excitation mechanism is called displacive. Before the short laser pulse hits the sample, the atoms are in their equilibrium state. If the incoming pump pulse is absorbed, the electronic distribution in the material will be changed, and the atoms will no longer be in their equilibrium state. They will move towards new equilibrium positions, causing atomic oscillations, which can be identified as coherent phonons [52].

The process following the almost instantaneous absorption process is rapid thermal-ization of the excited carriers via carrier-carrier scattering. In this fast process (typically a few tens of femtoseconds), electrons and holes thermalize with each other. This is followed by recombination. Auger recombination is the dominant mechanism, and is proportional to the square of the carrier density. At this time,

the lattice and electron temperatures are different and thus the carriers and the lattice thermalize. This process is called carrier lattice thermalization and starts with carrier-phonon scattering. The carriers thermalize with the lattice by emitting longitudinal optical phonons. As the process continues, the population of the optical phonons increases, resulting in phonon-phonon scattering. The optical phonons decay into two acoustic phonons, due to energy and momentum conservation [41]. This brings the lattice into local thermal equilibrium once more, and after a few tens of picoseconds most of the carriers are in thermal equilibrium with the lattice.

4.4 The Thomsen model

The model proposed by Thomsen et al. [53] is used to explain how a laser-generated strain pulse is launched into a solid. Here, the laser pulse is absorbed in a thin surface layer of the sample. The free carriers generated by the laser pulse cause electronic stress, and the increase in lattice temperature leads to thermal stress. The Thomsen model was used in this work as a simple model to fit experimental data. Therefore, electronic stress was neglected and the thermal stress was assumed to be instantaneous. The near-surface stress generated is then released as an acoustic wave, which propagates into the material at the speed of sound. The total energy deposited by the laser pulse per unit volume at a distance z (direction parallel to the surface normal) is given by the following expression:

$$W(z) = \frac{(1-R)Q}{A\xi} exp(-z/\xi) \tag{4.1}$$

where R is the reflectivity, Q is the energy of the light pulse, ξ is the absorption length, A is the illuminated area. The absorbed laser light results in rapid heating of the sample. Initially, heating occurs in a constant volume, meaning that only stress is created instantly. The stress is released via expansion, which triggers a strain wave that has the following form:

$$\eta(z,t) = \frac{(1-R)Q\beta}{AC\xi}\frac{1+\nu}{1-\nu}\left[e^{-\frac{z}{\xi}}\left(1-\frac{1}{2}e^{-\frac{vt}{\xi}}\right)-\frac{1}{2}e^{-|z-vt|/\xi_{sgn(z-vt)}}\right] \tag{4.2}$$

$$v = \sqrt{3\frac{1-\nu}{1+\nu}\frac{B}{\rho}} \tag{4.3}$$

where β is the linear expansion coefficient, C heat capacity, ν is the Poission's ratio, v is the longitudinal speed of sound, B is the bulk modulus, ρ is the density, sgn is the sign function. Fig. 4.2 shows strain as a function of depth for various times.
Close to the surface one can see the non-propagating part, which consists of thermal expansion that follows the exponential profile of the absorbed laser beam. The dynamic part, the acoustic wave, moves away from the surface. The width of the wave is about twice the absorption depth. The strain wave can be regarded as a distribution of coherent phonons, with the spectrum shown below in Fig. 4.3. Here one can see that some phonon modes are more populated than others.

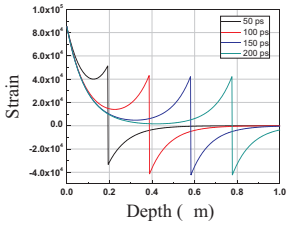

Figure 4.2: Simulated strain profile in an InSb crystal using the model described by Thomsen et al. at four points in time after laser excitation: 50 ps, 100 ps, 150 ps and 200 ps.

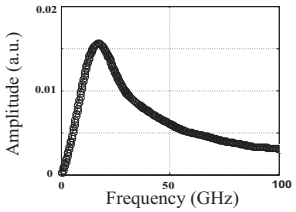

Figure 4.3: Fourier transform of a strain wave from a single laser pulse.

4.5 Ultrafast phase transitions

Short laser pulses enable the study of fast phase transitions often occurring on the time scale of a few picoseconds. For example, a transition known as non-thermal melting occurs in less than a picosecond. This has been observed in a number of materials [18], [54], [4]. The melting of a solid usually occurs when the thermal atomic vibrations become so energetic that the atomic bonds holding the atoms together break. In a liquid, the atoms move more freely and atomic bonds are easily created or broken. Thermal melting is a slow process since the atoms must gain sufficient kinetic energy, which takes time since carrier lattice thermalization is slow (many picoseconds). Another way of melting a sample is to break the bonds holding the atoms together directly with laser light. If a semiconductor is irradiated with an intense femtosecond laser pulse, and roughly 10% or more of the valence electrons are excited, then melting occurs. In other words, the intense laser pulse flattens the interatomic potential and the atoms move away from each other with the kinetic energy they had before melting. There is not yet a unified physical model to describe the early process of non-thermal melting, and different groups have proposed different explanations [5], [55], [56].

Chapter 5

Beamline D611 at MAX-lab

Almost all the experimental work described in this thesis was carried out at beamline D611 at the Swedish National Laboratory MAX-lab. The beamline is a bending magnet beamline dedicated to time-resolved studies. The X-ray source, the laser system and the fast detector used for the TXRD experiments are briefly described below.

5.1 The X-ray source

Beamline D611 at the MAX II electron storage ring is dedicated to laser-pump/X-ray probe experiments. MAX II is a third-generation synchrotron light source with 1.5 GeV electron energy and 90 m circumference, which has been in operation since 1996. X-rays are generated in a bending magnet and focused by a gold-coated toroidal mirror onto a 400 x 200 μm^2 spot with 7 x 0.7 $mrad^2$ divergence (horizontal x vertical). The beamline has a double-crystal monochromator equipped with InSb crystals and multilayer mirrors. The X-ray energy can be varied between 1.8 keV and 9 keV. The MAX-II storage ring provides 30 electron bunches separated by 10 ns (see Fig. 5.1). The ring can be operated in two modes: the even filling mode and the non-even filling mode. In the first case the electron bunches are very similar in size. This is the most common mode of operation. However, non-even filling is advantageous for time-resolved studies, because only a single electron bunch - the largest one - is used. The duration of the X-ray pulse resulting from a single electron bunch is about 700 ps. In order to perform time-resolved experiments with a high time resolution a fast detector is used. The beamline is equipped with a streak camera that has a temporal resolution better than one picosecond. The streak camera was used in most of the experiments performed at D611 and is described in detail in Section 5.3.

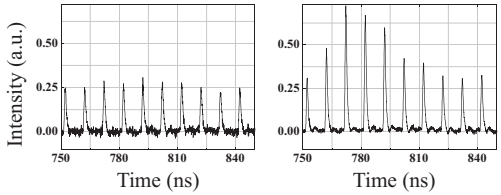

Figure 5.1: Part of an X-ray pulse train showing the two different operation modes of the MAX II storage ring: even filling mode (left) and non-even filling mode (right).

5.2 The laser system

Short laser pulses were generated by a passively mode-locked, titanium-doped sapphire oscillator followed by a cryogenically cooled $Ti : Al_2O_3$ multipass laser amplifier. The highest repetition rate of the amplifier is 10 kHz, but it was operated at 4.25 kHz. The short laser pulses from the oscillator were sent to the amplifier as seed pulses. The amplifier uses the chirped pulse amplification technique, meaning that the pulse is stretched before amplification and recompressed afterwards by a pair of gratings. The stretched laser pulse passes through the liquid-nitrogen-cooled $Ti : Al_2O_3$ crystal 11 times. The amplified and compressed laser pulse is then split into three parts see (Fig. 5.2).

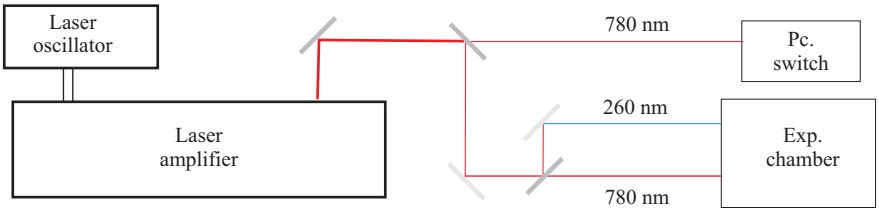

Figure 5.2: Schematic overview of the laser system.

About ten percent of the beam is sent to a photoconductive switch that is used to generate a fast voltage ramp. The remaining parts are used to excite the sample and to generate the UV beam that is sent directly to the streak camera cathode, where it serves as a temporal reference. The characteristics of the amplified laser pulse are listed in Table 5.1. In order to conduct time-resolved experiments, the laser system must be synchronized with the X-ray source, such that the laser pulse arrives at the sample as the same time as the X-rays. This is achieved by locking the oscillator to the radio frequency signal from the accelerating cavities of the synchrotron ring with a jitter below 30 ps. The repetition rate of the oscillator is determined by the length of the cavity. The end mirror in the oscillator is mounted on a translation stage, and a piezo element is glued to the top of the mirror. The piezo element is used for fast adjustments, while the translation stage is used to compensate for slow fluctuations.

Table 5.1: Typical laser pulse characteristics

Repetition rate	1 - 10 kHz
Pulse energy	1 mJ
Average power	4 W
Pulse duration	50 fs
Wavelength	780 nm

A small fast photodiode picks up the 100 MHz pulse train and sends it to a 100 MHz band pass filter, after which it is amplified. The signal from the storage ring is taken from the beam pick-up monitor sensor. It is also sent to a 100 MHz band pass filter, amplified and passed through a phase shifter, where an arbitrary phase shift can be added to introduce a delay between the laser and the X-rays. Since the delay between two X-ray pulses is 10 ns, a phase shift of 2π corresponds to a delay of 10 ns. The filtered and amplified electronic signals from the oscillator and the storage ring are mixed and an error signal is derived. This signal is used as feedback in a phase-lock loop. Frequency fluctuations are accounted for by changing the cavity length of the oscillator. The laser amplifier cannot work at 100 MHz, and its frequency is adjusted between 1 and 10 kHz. The trigger signal can be taken from the oscillator using the photodiode or from the X-ray signal.

5.3 The streak camera

Work has been performed using an in-house designed and constructed X-ray streak camera, when a time resolution better than 700 ps is required. A streak camera works in a similar way to an analogue oscilloscope, where time is converted into distance. The streak camera is shown schematically in Fig. 5.3.

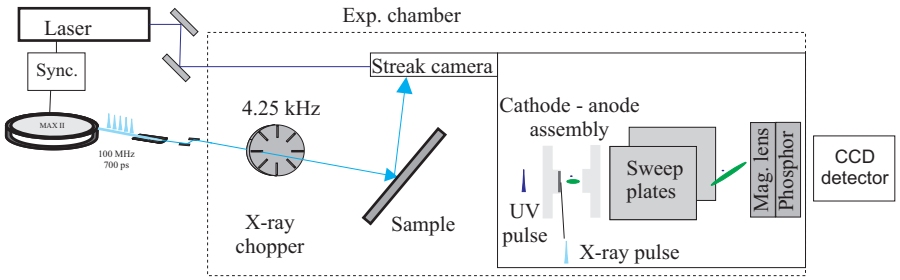

Figure 5.3: Working principle of the streak camera installed at D611.

The X-ray signal from the sample hits the CsI cathode. A cloud of photoelectrons is created via the photoelectric effect. The X-rays are incident on the cathode at grazing angle, in order to better match the X-ray penetration depth and the photo electron escape depth. The electrons are then accelerated towards the anode. They pass through a 100 μm wide anode slit and enter the space between two sweep plates.

A fast ramped voltage created by the laser pulse via a photoconductive switch deflects the electron beam. The deflected or streaked electrons pass through the electron focusing element and enter the multi-channel plate (MCP). Here they are amplified and projected onto a phosphor screen. The streaked image is then recorded using a charge coupled device (CCD) camera. The time resolution of the streak camera depends on a number of factors such as slit size, the electron transition time in the cathode-anode assembly, sweep speed and jitter. The energy spread of the photoelectrons depends on the material and has been measured for common cathode materials [57]. All these factors can be optimized to achieve sub-picosecond time resolution.

Chapter 6

Experiments

6.1 Time-resolved X-ray scattering from laser-molten indium antimonide

As non-thermal melting occurs a non-equilibrium liquid is created. Non-thermal melting occurs in less than 1 ps, and the thickness of the molten layer is a few tens of nanometres. The layer remains molten for a relatively long time, tens of nanoseconds, since there is a thick layer of hot solid InSb beneath it, and InSb has a high melting enthalpy. X-ray scattering from non-equilibrated liquid has been measured previously with femtosecond time resolution [58]. In the present work, it was found that this type of experiment can be performed at a synchrotron light source in repetitive mode (Paper I). The experimental set-up is shown in Fig. 6.2.

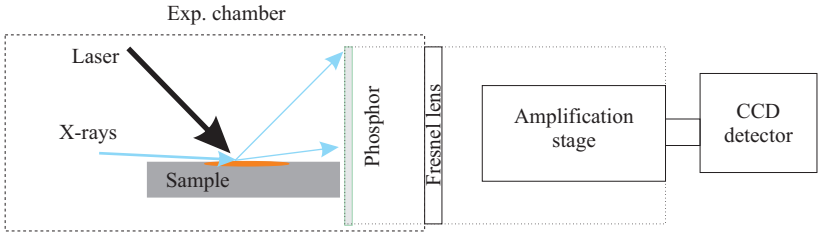

Figure 6.1: Schematic representation of the set-up used for the liquid X-ray scattering experiment.

The X-rays impinged at grazing incidence in order to match the laser melting depth and the X-ray probe depth. In this set-up a repetition rate of 4.25 kHz was used. The time resolution was limited by the duration of the X-ray pulse, and was around 300 ps. The X-rays scattered from the liquid impinge on a fast scintillator screen, where they are converted into visible light. The fast scintillator screen has a decay time of 2 ns, hence single X-ray pulses can be discriminated from the 100 MHz pulse train provided by the synchrotron light source. The visible light was then focused

by a Fresnel lens onto an image intensifier. Here the optical signal is converted into an electronic one, which is amplified and converted back into visible light. Finally, the signal is recorded with a CCD detector. Scattering from liquids is much weaker than that from a solid crystal. Therefore, the detector must be very efficient. The fast scintillator screen was coated with a thin layer of aluminium that reflects the photons that escape in the opposite direction, back towards the CCD detector. The laser-generated light was eliminated by covering the detector with thick aluminium foil. The amplification stage has two MCP stages. The first MCP is gateable, which allows the X-ray pulse that is synchronous with the laser to be selected. The quantum efficiency was increased by adding a second detector in series.
The measured time evolution of the laser-generated liquid was compared with data found in the literature, showing good agreement between the present work (Paper I) and that presented by others [58].

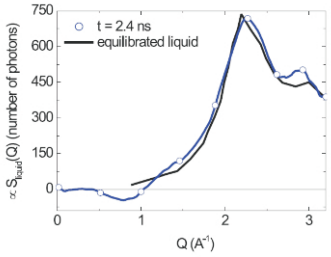

Figure 6.2: Measured structure of liquid InSb 2.4 ns after laser excitation (blue curve) compared with results found in the literature (black curve).

6.2 X-ray diffraction from the ripple structures created by femtosecond laser pulses

Static X-ray diffraction was used to investigate and characterize laser-induced surface structures on an asymmetrically cut InSb (110) crystal (Paper II). The experiment was carried out at beamline D611, MAX-lab in Lund.

M. Birnbaum et al. observed periodic surface structures when short, intense laser pulses with a laser fluence close to the melting threshold of the material interacted with the sample [59]. These spontaneous, highly periodic, permanent surface structures or "*ripples*" can be created on any solid material irradiated with pulsed or CW light. Most ripples run perpendicular to the incident electric field. At normal incidence the ripple spacing is close to or equal to the wavelength of the excitation light. It was found that ripples occur preferentially with three different periodic spacings given

by:

$$\Lambda_{\pm} = \frac{\lambda}{(1 \pm sin\theta)} \tag{6.1}$$

and

$$\Lambda_C = \frac{\lambda}{(cos\theta)} \tag{6.2}$$

where θ is the laser angle of incidence with respect to the surface, and λ is the wavelength of the laser radiation. The rippled surface structures were first explained by Emmony et al. [60] as interference between the incident laser light and light scattered by imperfections on the sample surface, such as dust or scratches. This interference causes intensity modulation, which in turn leads to inhomogeneous deposition of the energy. The wavelength, polarization and incident angle of the laser radiation determine the spatial period. So-called S^+ and S^- ripples occur perpendicularly to the polarization, while c-type fringes, which run parallel to the direction of polarization, are rarely formed. S^- ripples are usually dominant. A possible ripple formation mechanism from the liquid phase was proposed by Kerr et al. and is illustrated schematically in Fig. 6.3 [61].

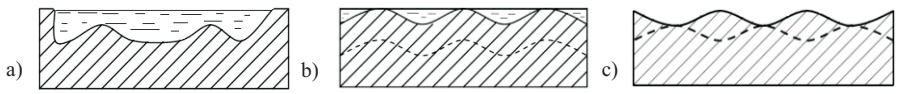

Figure 6.3: Schematic representation of ripple formation from liquid.

If the material is irradiated with an average fluence close to the melting threshold, some parts will be subjected to higher fluences and melt. Since density of the liquid InSb higher the level of the liquid is below solid surface (Fig. 6.3 a)). Since the transverse transport of energy is slow, the solid/liquid interface maps the inhomogeneous energy deposition due to interference and retains a sine like contour. During the re-solidification process the sine-like contour grows until its peaks reach the surface. The molten material gets locked in and the peaks cannot grow anymore. At this point, the liquid and solid regions are separate (Fig. 6.3 b)). As the liquid parts solidify they rise up and form a rippled surface.

In the present work (Paper II), an InSb wafer was placed in the experimental chamber and exposed to femtosecond laser pulses with a fluence up to 100 mJ/cm^2 and varying laser incidence angles. In order to compensate for the variation in the laser footprint on the InSb sample with incidence angle, different exposure times were used for different laser incidence angles such that the total accumulated fluence was constant. To ensure that the probe depth matched the thickness of the laser-irradiated surface layer the X-rays impinged at grazing incidence. X-ray reflectivity curves were recorded. The modified sample surface was then studied with an OM and

an AFM. The data from these measurements were used to simulate X-ray reflectivity curves from the laser-modified surface. It was found that the reflectivity curves were asymmetric in the areas irradiated by the laser. The shape and width of the rocking curve provide information about the morphology of the crystal. For laser fluences above the melting threshold the laser melts a thin surface layer on the sample. The thin molten layer regrows and regains a crystalline structure. At high laser fluences the crystal structure is permanently destroyed, and the X-ray reflectivity is therefore dramatically decreased.

Our group has developed a model that can simulate X-ray reflectivity curves in a few steps. First, information about the ripple height and periodicity are extracted from irradiated samples using the OM and AFM. The local variations in the angle of asymmetry are then calculated. These arise from the ripple structure, which periodically changes the surface orientation with respect to the lattice planes. X-ray reflectivity curves were calculated for each asymmetry angle. The average reflectivity curve is then calculated using the asymmetry angles occurrence as weight. Finally, it is assumed that there is a thin layer of amorphous material on top of the structure reducing the overall reflectivity. Good agreement was found between the model and the measured data (see Fig. 6.4).

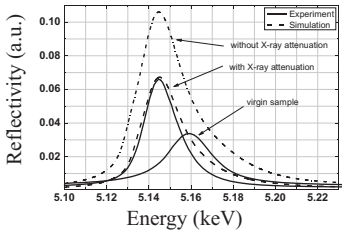

Figure 6.4: Simulated energy scans from the rippled InSb surface, together with an experimentally determined curve for comparison.

It was found that laser-generated surface structures can efficiently increase X-ray reflectivity. This must be taken into account when performing melting experiments in repetitive mode. The laser-created structures on the surface grow with exposure time. In order to avoid this effect the sample must be constantly translated.

6.3 Picosecond time-resolved X-ray refectivity of a laser heated amorphous carbon film

The laser pump/X-ray probe technique was used to measure the temporal evolution of a laser-heated amorphous carbon film on a Si crystal (Paper III). Amorphous carbon is used as a coating layer on X-ray mirrors for FELs such as the European X-ray Free Electron Laser, XFEL in Germany/Hamburg. Knowledge on expansion and changes in surface roughness is important in the further development of X-ray mirrors. Time-resolved X-ray reflectivity measurements were performed with a time

resolution of a few hundred picoseconds. The experiment was carried out at beamline ID09B at the European Synchrotron Radiation Facility (ESRF) in Grenoble, France. The beamline is dedicated to time-resolved X-ray studies. The beamline provides 1010 X-ray photons in a few hundreds of picoseconds at 986.3 Hz [62].
The experimental set-up is illustrated in Fig. 6.5. The sample was excited with a laser fluence below the damage threshold. The fast chopper is able to single out a single bunch of X-rays which is used to probe the sample. The X-ray incidence angle was scanned while following the time evolution of the excited sample, by changing the delay between the pump and the probe.

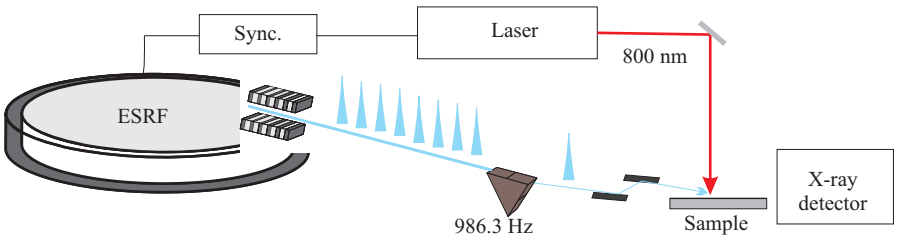

Figure 6.5: Experimental set-up used to study an amorphous carbon film at ESRF.

The dynamics in the laser-excited amorphous film was measured with a time resolution of 200 ps (Paper III), and the results are presented in Fig. 6.6, where the increase in thickness due to thermal expansion can be extracted. As a result of this, the density is reduced. An increase in surface roughness was also observed, which can be explained by inhomogeneous heating due to intensity variations in the laser footprint.

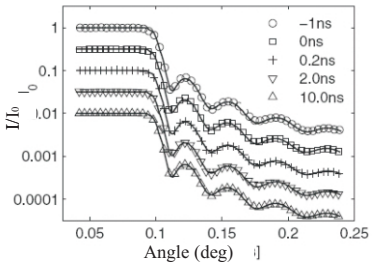

Figure 6.6: X-ray specular reflectivity from an amorphous carbon film at different delays between laser excitation and the X-ray probe.

6.4 Picosecond dynamics of laser-induced strain in graphite.

Paper IV describes measurements of the strain propagation in a laser-excited graphite film. This presented a considerable challenge, as it is difficult to study materials with low atomic numbers using X-rays due to their low scattering power. However, some of the results presented by Carbone et al. were confirmed, while others were not [63], [64]. The experiment was carried out at the FEMTO slicing beamline of the Swiss Light Source (SLS) in Villigen. The beamline produces X-ray pulses a few hundred femtoseconds long. These short X-ray pulses are generated when the electron beam interacts with strong laser radiation. This is illustrated schematically in Fig. 6.7.

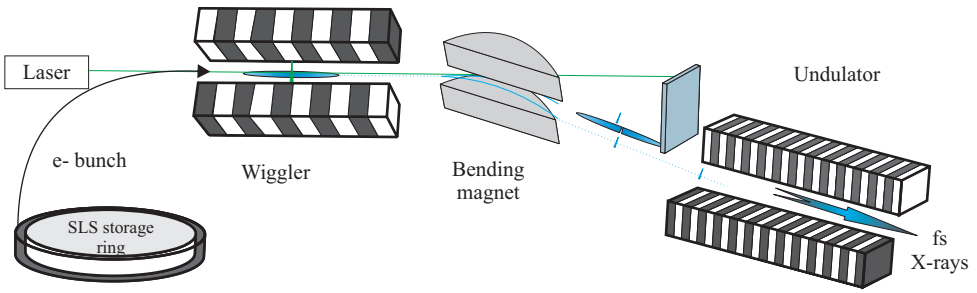

Figure 6.7: X-ray slicing at SLS.

X-ray slicing can be explained in three steps. The kinetic energy in the few-hundred-picosecond-long electron bunch is modulated with the aid of a short, intense laser pulse inside a wiggler, which is tuned to allow the transfer of energy from the light to the electrons. In this case, the energy of a small fraction of the electron bunch is modulated, meaning that they have a greater energy spread than normal. The electron bunch then passes through a dispersive element (bending magnet). Here, the modulated electrons are separated from the non-modulated ones, since they have a slightly different energy and thus a different radius in the magnetic field. Finally, the separated electron slice is sent to an insertion device (undulator), where X-rays are generated. The short X-ray pulses at the SLS are about 200 fs.

The X-rays impinged on the sample at a grazing angle in order to match the pump and probe depth. Thomsen's model was used to analyse the data, again neglecting electronic strain. The finite time for electron-lattice coupling was introduced phenomenologically and the strain profile was calculated numerically. The X-ray reflectivity was calculated using the dynamical theory of diffraction taking the strain into account. The recorded dynamics are presented as the difference between the

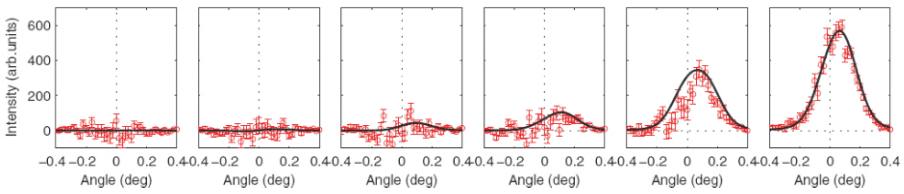

Figure 6.8: Differences in rocking curves at different delays between laser excitation and X-ray probe.

unperturbed rocking curve at different points in time (see Fig. 6.8). The strain was measured in the direction of the c-axis showing an expansion of about 2.8%. This comes from comparison with the simulations.

6.5 Generating and probing acoustic phonons in semiconductor nanostructures

Time-resolved X-ray diffraction was used to investigate InSb nanowires grown on an InAs substrate (Paper V). The aim was to study acoustic phonon propagation in the nanowires and to determine whether the acoustic propagation velocity in these structures is different from that in the bulk material, as predicted by Mingo et al. [65]. Phonons in bulk semiconductors have previously been studied using the same technique by Larsson et al. and Lindenberg et al. [42], [43]. Experimental verification of the reduction of the speed of sound in nanowires is necessary as this is important in many applications. The (111) reflection planes were used, which are parallel to the surface of the substrate with a Bragg angle of 59°. A large Bragg angle was chosen in order to obtain a narrow X-ray reflectivity curve. The laser excitation was normal to the surface of the substrate. The experimental geometry and the set-up are illustrated in Fig. 6.9. The laser system was synchronized to a single electron bunch in the MAX II storage ring with a jitter of 30 ps.

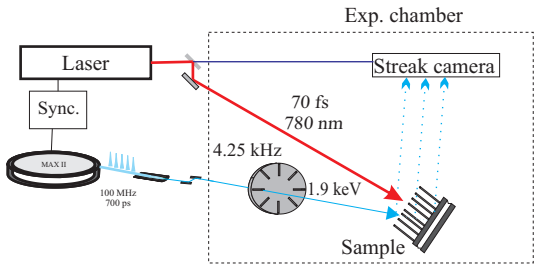

Figure 6.9: Experimental set-up used to study acoustic propagation in InSb nanowires.

The diffracted signal from the sample was sent to the streak camera described above. The repetition rate of the camera was set to 4.25 kHz with a time resolution of 10 ps, which was limited by the anode slit size and the sweep speed [66]. The laser excitation was periodically turned on and off in order to obtain the reflectivities with and without the laser, R_{on} and R_{off}, from which the normalized difference signal $(R_{on} - R_{off})/R_{off}$ was extracted. Two samples were tested, one 40 nm in diameter and one 80 nm in diameter. The length of both samples was about 1 μm. They were grown by MOVPE using trimethyl indium, trimethyl antimony and arsenic precursors on an InAs (111) substrate prepared with Au nanoparticles. The density of the nanowires on the surface was 5 per μm^2. The X-ray diffraction signal from the nanowires was weak because of the low nanowire density and the fact that the probing depth exceeded the pump depth by about a factor of five. The reflectivity curve and a SEM image of the sample are shown in Fig. 6.10

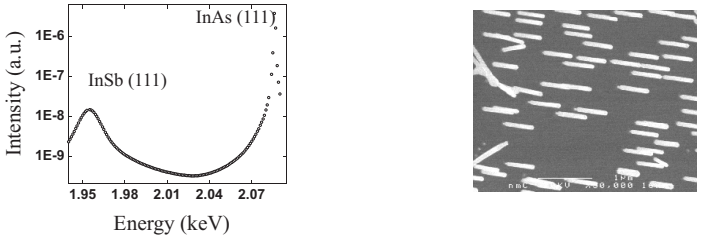

Figure 6.10: Reflectivity curve from the InAs/Sb nanowire sample and the SEM image of the sample itself.

X-ray diffraction is a powerful technique for detecting strain through changes in the Bragg condition. The shape of the reflectivity curve can provide a great deal of information about the structure being probed. The amplitude of the reflection curve is sensitive to the temperature via the Debye-Waller factor, and the position of the peak is sensitive to strain via Bragg's law. The experiment is based on Thomsen's model, which assumes that the energy from the laser is converted into heat near the upper surface. The travelling strain wave modifies the interplanar distance. It can be decomposed into (coherently excited) phonon modes. Each excited phonon mode represents an additional periodicity of the lattice. The coherently excited phonon modes add "wings" to the reflection curve. By tuning ΔE (energy offset) it is possible to select the phonon wave vector q given by the modified Laue condition: $k - k_0 = G \pm q$ with $q = 2\Delta k sin\theta$. Here k_0 and k are the wave vectors of the incident and the reflected X-ray waves, respectively, and q is the phonon wave vector. This is shown schematically in Fig. 6.11. Firstly, phonons were probed in the substrate to ensure spatial and temporal overlap. This was done by tuning the X-ray energy to fulfil the Bragg condition for InAs. The evolution of the signal was recorded and is shown in Fig. 6.12.
Here, two phonon modes were selected via the choice of ΔE, such that the oscillation periods were T and $2T$, respectively. The dominant frequency can be extracted by applying a Fourier transform. Knowing the frequency, ω, and the modulus of q, gives the speed of sound: $v = \omega/q$. Fig. 6.13 shows ω as a function of q for different values

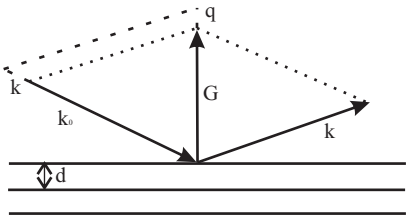

Figure 6.11: Vector representation of the Bragg law.

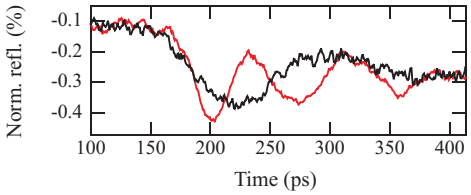

Figure 6.12: X-ray reflectivity after excitation by a single laser pulse at two energy offsets.

of ΔE. The slope of the straight line provides the speed of sound. The speed of sound in bulk InAs in the [111] direction is known to be 4400 m/s [67]. The slope of the line in Fig. 6.13 gives a value of 4200 m/s.

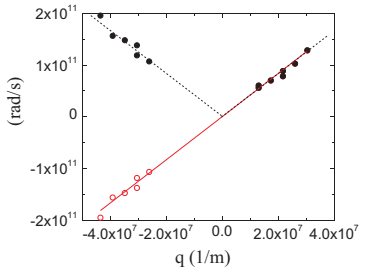

Figure 6.13: A graph showing the frequency, ω, vs. the phonon wave vector q for bulk InAs. The slope gives the speed of sound in the material (4200 m/s).

The X-ray photon energy was then tuned to fulfil the Bragg condition in InSb. In order to investigate whether the nanowires could be excited with the laser, different laser fluences between 1 and 10 were tested. A response to the incident laser light was observed for all fluences, as shown in Fig. 6.14.
Immediately after laser excitation the reflection curve shifts towards lower energies, corresponding to lattice expansion. A large initial strain builds up during the first

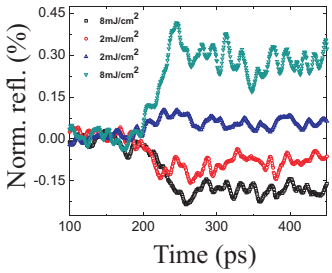

Figure 6.14: X-ray reflectivity from a nanowire sample using different laser fluences.

50 ps, and partial relaxation is observed after about 200 ps. This is very pronounced at high fluences. The signal before and after laser excitation is used to estimate the temperature in the nanowires. It was found that the temperature after exposure to a fluence of 5 mJ/cm^2 was about 500 K. As can be seen, the amplitude of the signal increases with increasing incident fluence. A further increase in incidence fluence leads to permanent sample damage. The heat conduction in nanowires is different from that in bulk material [40], [29] in that heat dissipation is slower in nanowires, and the damage threshold could therefore be lower than in the bulk. The laser damage threshold for InSb nanowires was found to be around 6 mJ/cm^2. Since X-ray scattering from nanowires is weak diffracted signal is noisy. However periodic phonon oscillations can be observed (see Fig. 6.15).

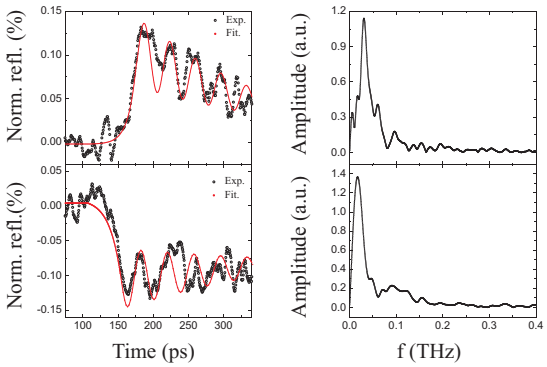

Figure 6.15: X-ray reflectivity from InSb nanowires after excitation with a single laser pulse (left) and the Fourier transform (right).

The speed of sound in InSb nanowires was found to be about v(111) = 2800 (70) m/s, which is lower than the value of 3880 m/s in bulk material. According to Mingo et al. [65] there should be a dramatic reduction in the velocity of sound in nanowires, and the velocity decreases with decreasing wire radius. Our findings confirm this. In Fig. 6.16 phonon frequency versus phonon wave vector in InSb nanowires is shown .

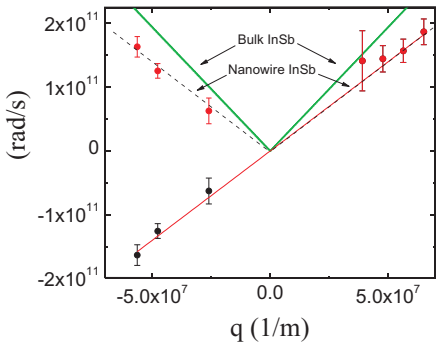

Figure 6.16: Frequency ω vs. phonon wave vector, q, in InSb nanowires. The velocity of sound is 2800 m/s, i.e. considerably smaller than in the bulk material.

Chapter 7

Outlook

X-ray scattering techniques are the standard tool for material characterization and structure determination. However, it is difficult to implement complex systems and time-resolved techniques at third-generation light sources. This is mainly due to the length of the X-ray pulses and the relatively low X-ray flux. A typical X-ray pulse duration at a third-generation light source is a few hundred picoseconds, which limits the possibility of studying slow processes or high-reflectivity materials. Shorter X-ray pulses can be produced at synchrotron light sources at the cost of X-ray flux. This means that the samples must be highly scattering or that long exposure times must be used. Nano-structures such as nanowires and quantum dots or single proteins are very difficult or impossible to study at third-generation light sources due to their small scattering power and the relatively large X-ray footprint. One way of overcoming this limitation is to use fourth-generation light sources such as an FEL. Two hard X-ray FELs are currently in operation: the LCLS in the USA (opened in 2009) and SACLA in Japan (opened in 2011). These machines provide short X-ray pulses at high flux that can be used for time-resolved X-ray studies. The European FEL in Germany will be operational in 2015, and will be the brightest X-ray source in the world. The X-ray pulse duration provided by an FEL is a few femtoseconds, meaning that fast atomic processes, such as chemical reactions, phase transitions and lattice dynamics, can be studied. Time-resolved studies on nanowires have been performed mainly at the D611 beamline at the MAX II facility. However, the signal was low due to low flux from the source and a large X-ray footprint. Typical acquisition times for these measurements were around 8 hours. The same studies could be done in seconds at an FEL. Such experiments are highly relevant since nanowires have very interesting and different properties from bulk material. For instance, heat transport gradually decreases with nanowire diameter. Many other questions are waiting to be answered, for example, How different is the speed of sound is in nanowires? How low can it be? Can we create a structure that allows phononic and electronic heat transport to be separated in nanowires? It is important to find answers to all these questions, if we are to realize nanowire thermoelectric devices.

References

[1] D. Dunstan, H. Colson, and A. Kimber, "Analysis of high-resolution x-ray diffraction in semiconductor strained layers," *JOURNAL OF APPLIED PHYSICS*, vol. 86, no. 2, pp. 782 – 790, 1999.

[2] A. Darahanau, A. Nikulin, R. Dilanian, and B. Muddle, "X-ray diffraction profiling of metal-metal interfaces at the nanoscale," *PHYSICAL REVIEW B*, vol. 75, no. 7, pp. 75416 – 1, 2007/02/15.

[3] P. Yang, R. Yan, and M. Fardy, "Semiconductor nanowire: Whats next?," *NANO LETTERS*, vol. 10, no. 5, pp. 1529 – 1536, 2010.

[4] K. Sokolowski-Tinten, J. Bialkowski, M. Boing, A. Cavalleri, and D. von der Linde, "Thermal and nonthermal melting of gallium arsenide after femtosecond laser excitation," *PHYSICAL REVIEW B*, vol. 58, pp. 11805–11808, NOV 1 1998.

[5] A. Lindenberg, J. Larsson, K. Sokolowski-Tinten, K. Gaffney, C. Blome, O. Synnergren, J. Sheppard, C. Caleman, A. MacPhee, D. Weinstein, D. Lowney, T. Allison, T. Matthews, R. Falcone, A. Cavalieri, D. Fritz, S. Lee, P. Bucksbaum, D. Reis, J. Rudati, P. Fuoss, C. Kao, D. Siddons, R. Pahl, J. Als-Nielsen, S. Duesterer, R. Ischebeck, H. Schlarb, H. Schulte-Schrepping, T. Tschentscher, J. Schneider, D. von der Linde, O. Hignette, F. Sette, H. Chapman, R. Lee, T. Hansen, S. Techert, J. Wark, M. Bergh, G. Huldt, D. van der Spoel, N. Timneanu, J. Hajdu, R. Akre, E. Bong, P. Krejcik, J. Arthur, S. Brennan, K. Luening, and J. Hastings, "Atomic-scale visualization of inertial dynamics," *SCIENCE*, vol. 308, pp. 392–395, APR 15 2005.

[6] E. P. Ed, *International Tables of Crystallography, Vol. C.* Springer, Berlin, 2004.

[7] P. Sondhauss Model (coins) that uses dynamical diffraction theory to simulate X-ray reflectivity curves. Developed by Peter Sondhauss and available to the group.

[8] B. E. Warren, *X-ray diffraction.* Dover publications, 1990.

[9] A. Authier, *Dynamical Theory of X-Ray Diffraction.* Oxford University Press, USA, 2003.

[10] http://www.esrf.eu/computing/scientific/xop2.1/.

[11] http://sergey.gmca.aps.anl.gov/.

[12] D. Aspnes and A. Stunda, "Dielectric functions and optical-parameters of si, ge, gap, gaas, gasb, inp, inas, and insb from 1.5 to 6.0 ev," *PHYSICAL REVIEW B*, vol. 27, no. 2, pp. 985–1009, 1983.

[13] D. McMorrow and J. Als-Nielsen, *Elements of Modern X-ray physics.* John Wiley and Sons Ltd, New york 2001.

[14] J. Wang, M. W. Graham, Y. Ma, G. R. Fleming, and R. A. Kaindl, "Ultrafast Spectroscopy of Midinfrared Internal Exciton Transitions in Separated Single-Walled Carbon Nanotubes," *PHYSICAL REVIEW LETTERS*, vol. 104, APR 30 2010.

[15] A. Zewail, "Femtochemistry. Past, present, and future," *PURE AND APPLIED CHEMISTRY*, vol. 72, pp. 2219–2231, DEC 2000. 15th International Conference on Physical Organic Chemistry (ICPOC 15), GOTHENBURG, SWEDEN, JUL 08-13, 2000.

[16] J. Ditusa, K. Lin, M. Park, M. Isaacson, and J. Parpia, "Role of phonon dimensionality on electron-phonon scattering rates," *PHYSICAL REVIEW LETTERS*, vol. 68, pp. 1156–1159, FEB 24 1992.

[17] R. Ito, H. Kawamura, and M. Fukai, "Anisotropic phonon scattering of electrons in germanium and silicon," *PHYSICS LETTERS*, vol. 13, no. 1, pp. 26–27, 1964.

[18] C. Siders, A. Cavalleri, K. Sokolowski-Tinten, C. Toth, T. Guo, M. Kammler, M. von Hoegen, K. Wilson, D. von der Linde, and C. Barty, "Detection of nonthermal molting by ultrafast X-ray diffraction," *SCIENCE*, vol. 286, pp. 1340–1342, NOV 12 1999.

[19] A. Rousse, C. Rischel, S. Fourmaux, I. Uschmann, S. Sebban, G. Grillon, P. Balcou, E. Foster, J. Geindre, P. Audebert, J. Gauthier, and D. A. Hulin, "Nonthermal melting in semiconductors measured at femtosecond resolution," *NATURE*, vol. 410, pp. 65–68, MAR 1 2001.

[20] K. Sokolowski-Tinten, C. Blome, C. Dietrich, A. Tarasevitch, M. von Hoegen, D. von der Linde, A. Cavalleri, J. Squier, and M. A. A. Kammler, "Femtosecond x-ray measurement of ultrafast melting and large acoustic transients," *PHYSICAL REVIEW LETTERS*, vol. 87, pp. art. no.–225701, NOV 26 2001.

[21] S. Tongay, E. Durgun, and S. Ciraci, "Atomic strings of group IV, III-V, and II-VI elements," *APPLIED PHYSICS LETTERS*, vol. 85, pp. 6179–6181, DEC 20 2004.

[22] https://slacportal.slac.stanford.edu/.

[23] J. Gaudin, B. Keitel, A. Jurgilaitis, R. Nüske, L. Guérin, J. Larsson, K. Mann, B. Schäfer, K. Tiedtke, A. Trapp, T. Tschentscher, F. Yang, M. Wulff, H. Sinn, and B. Flöter, "Time-resolved investigation of nanometer scale deformations induced by a high flux x-ray beam," *OPTICS EXPRESS*, vol. 19, pp. 15516–15524, Aug 2011.

[24] C. Siders and A. Cavalleri, "Creating transient crystal structures with light," *SCIENCE*, vol. 300, pp. 591–592, APR 25 2003.

[25] A. Gibaud and S. Hazra, "X-ray reflectivity and diffuse scattering," *CURRENT SCIENCE*, vol. 78, pp. 1467–1477, JUN 25 2000.

[26] R. Nuske, A. Jurgilaitis, H. Enquist, S. D. Farahani, J. Gaudin, L. Guerin, M. Harb, C. v. K. Schmising, M. Stoermer, M. Wulff, and J. Larsson, "Picosecond time-resolved x-ray refectivity of a laser-heated amorphous carbon film," *APPLIED PHYSICS LETTERS*, vol. 98, MAR 7 2011.

[27] H. Frederikse and E. Mielczarek, "Thermoelectric power of indium antimonide," *PHYSICAL REVIEW*, vol. 99, no. 6, pp. 1889–1890, 1955.

[28] N. Mingo, "Thermoelectric figure of merit and maximum power factor in III-V semiconductor nanowires," *APPLIED PHYSICS LETTERS*, vol. 84, pp. 2652–2654, APR 5 2004.

[29] A. I. Hochbaum, R. Chen, R. D. Delgado, W. Liang, E. C. Garnett, M. Najarian, A. Majumdar, and P. D. Yang, "Enhanced thermoelectric performance of rough silicon nanowires," *NATURE*, vol. 451, pp. 163–U5, JAN 10 2008.

[30] P. J. Pauzauskie and P. Yang, "Nanowire photonics," *MATERIALS TODAY*, vol. 9, pp. 36–45, OCT 2006.

[31] R. Yan, D. Gargas, and P. Yang, "Nanowire photonics," *NATURE PHOTONICS*, vol. 3, pp. 569–576, OCT 2009.

[32] J. Johansson, B. Wacaser, K. Dick, and W. Seifert, "Growth related aspects of epitaxial nanowires," *NANOTECHNOLOGY*, vol. 17, pp. S355–S361, JUN 14 2006.

[33] N. W. Ashcroft and N. D. Mermin, *Solid State Physics*. Harcourt College Publishers, 1976.

[34] T. Ito, "Simple criterion for wurtzite-zinc-blende polytypism in semiconductors," *JAPANESE JOURNAL OF APPLIED PHYSICS PART 2-LETTERS*, vol. 37, pp. L1217–L1220, OCT 15 1998.

[35] T. Akiyama, K. Sano, K. Nakamura, and T. Ito, "An empirical potential approach to wurtzite-zinc-blende polytypism in group III-V semiconductor nanowires," *JAPANESE JOURNAL OF APPLIED PHYSICS PART 2-LETTERS & EXPRESS LETTERS*, vol. 45, pp. L275–L278, MAR 2006.

[36] P. Caroff, J. B. Wagner, K. A. Dick, H. A. Nilsson, M. Jeppsson, K. Deppert, L. Samuelson, L. R. Wallenberg, and L.-E. Wernersson, "High-quality InAs/InSb nanowire heterostructures grown by metal-organic vapor-phase epitaxy," *SMALL*, vol. 4, pp. 878–882, JUL 2008.

[37] R. Wagner and W. Ellis, "Vapor-liquid-solid mechanism of single crystal growth (new method growth catalysis from impurity whisker epitaxial + large crystals si e)," *APPLIED PHYSICS LETTERS*, vol. 4, no. 5, pp. 89–&, 1964.

[38] V. Schmidt and U. Goesele, "How nanowires grow," *SCIENCE*, vol. 316, pp. 698–699, MAY 4 2007.

[39] G. Mahan and J. Sofo, "The best thermoelectric," *PROCEEDINGS OF THE NATIONAL ACADEMY OF SCIENCES OF THE UNITED STATES OF AMERICA*, vol. 93, pp. 7436–7439, JUL 23 1996.

[40] L. Hicks and M. Dresselhaus, "Thermoelectric figure of merit of a one-dimensional conductor," *PHYSICAL REVIEW B*, vol. 47, pp. 16631–16634, JUN 15 1993.

[41] *J.M. Ziman: Electrons and Phonons (Oxford University Press, Oxford 1967).*

[42] J. Larsson, A. Allen, P. Bucksbaum, R. Falcone, A. Lindenberg, G. Naylor, T. Missalla, D. Reis, K. Scheidt, A. Sjogren, P. Sondhauss, M. Wulff, and J. Wark, "Picosecond X-ray diffraction studies of laser-excited acoustic phonons in InSb," *APPLIED PHYSICS A-MATERIALS SCIENCE & PROCESSING*, vol. 75, pp. 467–478, OCT 2002.

[43] A. Lindenberg, I. Kang, S. Johnson, T. Missalla, P. Heimann, Z. Chang, J. Larsson, P. Bucksbaum, H. Kapteyn, H. Padmore, R. Lee, J. Wark, and R. Falcone, "Time-resolved X-ray diffraction from coherent phonons during a laser-induced phase transition," *PHYSICAL REVIEW LETTERS*, vol. 84, pp. 111–114, JAN 3 2000.

[44] H. Jeschke, M. Garcia, and K. Bennemann, "Theory for the ultrafast ablation of graphite films," *PHYSICAL REVIEW LETTERS*, vol. 87, JUL 2 2001.

[45] A. Kaplan, M. Lenner, and R. E. Palmer, "Emission of ions and charged clusters due to impulsive Coulomb explosion in ultrafast laser ablation of graphite," *PHYSICAL REVIEW B*, vol. 76, AUG 2007.

[46] T. Windhorst and G. Blount, "Carbon-carbon composites: a summary of recent developments and applications," *MATERIALS & DESIGN*, vol. 18, no. 1, pp. 11–15, 1997.

[47] J. M. Schnorr and T. M. Swager, "Emerging Applications of Carbon Nanotubes," *CHEMISTRY OF MATERIALS*, vol. 23, pp. 646–657, FEB 8 2011.

[48] J. Zou and A. Balandin, "Phonon heat conduction in a semiconductor nanowire," *JOURNAL OF APPLIED PHYSICS*, vol. 89, pp. 2932–2938, MAR 1 2001.

[49] G.-Y. Huang and Y.-L. Kang, "Acoustic vibrations of a circular nanowire by considering the effect of surface," *JOURNAL OF APPLIED PHYSICS*, vol. 110, JUL 15 2011.

[50] B. E. A. Saleh and M. C. Teich, *Fundamentals of Photonics*. Wiley-Interscience, 2007.

[51] E. Yoffa, "Dynamics of dense laser-induced plasmas," *PHYSICAL REVIEW B*, vol. 21, no. 6, pp. 2415–2425, 1980.

[52] H. Zeiger, J. Vidal, T. Cheng, E. Ippen, G. Dresselhaus, and M. Dresselhaus, "Theory for displacive excitation of coherent phonons," *PHYSICAL REVIEW B*, vol. 45, pp. 768–778, JAN 1 1992.

[53] C. Thomsen, H. Grahn, H. Maris, and J. Tauc, "Surface generation and detection of phonons by picosecond light-pulses," *PHYSICAL REVIEW B*, vol. 34, pp. 4129–4138, SEP 15 1986.

[54] H. Enquist, H. Navirian, T. N. Hansen, A. M. Lindenberg, P. Sondhauss, O. Synnergren, J. S. Wark, and J. Larsson, "Large acoustic transients induced by nonthermal melting of InSb," *PHYSICAL REVIEW LETTERS*, vol. 98, JUN 1 2007.

[55] C. Shank, R. Yen, and C. Hirlimann, "Time-resolved reflectivity measurements of femtosecond-optical-pulse induced phase-transitions in silicon," *PHYSICAL REVIEW LETTERS*, vol. 50, no. 6, pp. 454–457, 1983.

[56] E. S. Zijlstra, J. Walkenhorst, and M. E. Garcia, "Anharmonic noninertial lattice dynamics during ultrafast nonthermal melting of InSb," *PHYSICAL REVIEW LETTERS*, vol. 101, SEP 26 2008.

[57] B. Henke, J. Knauer, and K. Premaratne, "The characterization of x-ray photocathodes in the 0.1-10-kev photon energy region," *JOURNAL OF APPLIED PHYSICS*, vol. 52, no. 3, pp. 1509 – 20.

[58] A. M. Lindenberg, S. Engemann, K. J. Gaffney, K. Sokolowski-Tinten, J. Larsson, P. B. Hillyard, D. A. Reis, D. M. Fritz, J. Arthur, R. A. Akre, M. J. George, A. Deb, P. H. Bucksbaum, J. Hajdu, D. A. Meyer, M. Nicoul, C. Blome, T. Tschentscher, A. L. Cavalieri, R. W. Falcone, S. H. Lee, R. Pahl, J. Rudati, P. H. Fuoss, A. J. Nelson, P. Krejcik, D. P. Siddons, P. Lorazo, and J. B. Hastings, "X-ray diffuse scattering measurements of nucleation dynamics at femtosecond resolution," *PHYSICAL REVIEW LETTERS*, vol. 100, APR 4 2008.

[59] M. Birnbaum, "Semiconductor surface damage produced by ruby lasers," *JOURNAL OF APPLIED PHYSICS*, vol. 36, no. 11, pp. 3688–&, 1965.

[60] D. Emmony, R. Howson, and L. Willis, "Laser mirror damage in germanium at 10.6 mu," *APPLIED PHYSICS LETTERS*, vol. 23, no. 11, pp. 598–600, 1973.

[61] N. Kerr, B. Omar, S. Clark, and D. Emmony, "The topography of laser-induced ripple structures," *JOURNAL OF PHYSICS D-APPLIED PHYSICS*, vol. 23, pp. 884–889, JUL 14 1990.

[62] M. Cammarata, L. Eybert, F. Ewald, W. Reichenbach, M. Wulff, P. Anfinrud, F. Schotte, A. Plech, Q. Kong, M. Lorenc, B. Lindenau, J. Raebiger, and S. Polachowski, "Chopper system for time resolved experiments with synchrotron radiation," *REVIEW OF SCIENTIFIC INSTRUMENTS*, vol. 80, JAN 2009.

[63] F. Carbone, P. Baum, P. Rudolf, and A. H. Zewail, "Structural preablation dynamics of graphite observed by ultrafast electron crystallography," *PHYSICAL REVIEW LETTERS*, vol. 100, JAN 25 2008.

[64] H. Park and J. M. Zuo, "Direct measurement of transient electric fields induced by ultrafast pulsed laser irradiation of silicon," *APPLIED PHYSICS LETTERS*, vol. 94, JUN 22 2009.

[65] N. Mingo and D. Broido, "Lattice thermal conductivity crossovers in semiconductor nanowires," *PHYSICAL REVIEW LETTERS*, vol. 93, DEC 10 2004.

[66] H. Enquist, H. Navirian, R. Nuske, C. v. K. Schmising, A. Jurgilaitis, M. Herzog, M. Bargheer, P. Sondhauss, and J. Larsson, "Subpicosecond hard x-ray streak camera using single-photon counting," *OPTICS LETTERS*, vol. 35, pp. 3219–3221, OCT 1 2010.

[67] http://www.ioffe.ru/SVA/NSM/Semicond/index.html.

Comments on my participation in the studies

In addition to the work presented in this thesis, I have spent a large amount of time on improving the beamline control software and developing the streak camera at the D611 beamline. I wrote the control program for translating the cryostat in three directions. This was later integrated into the main control program of beamline D611. I participated in the implementation of the detector for the liquid scattering experiment. I made a significant contribution to the preparation of upcoming experiments, including sample preparation and testing. I have investigated the optical reflectivity from the sample and the laser damage thresholds. I studied sample surfaces using an OM and an SEM. During the course of my work the design of the streak camera cathode has been improved, and better streak camera performance in terms of higher quantum efficiency has been achieved.

Paper I

This paper describes time-resolved X-ray scattering from a laser-generated non-equilibrium liquid. I participated in constructing the detection system and in the data acquisition, and contributed to the data analysis.

Paper II

This paper describes how a short laser pulse, powerful enough to melt the sample surface, modifies the surface structure of the sample (causing ripples). I was the person mainly responsible for the experiment, I carried out most of the data analysis and wrote the first draft of the paper.

Paper III

This paper presents a method that can be used to characterize thin films after laser excitation with picosecond time resolution. Time-resolved specular X-ray reflectivity was used to follow the dynamics of an excited amorphous carbon film on a Si substrate. I participated in the experiment, and contributed to the data analysis and

the preparation of the manuscript.

Paper IV

In this paper, the picosecond dynamics of laser-excited natural graphite is presented. Laser-generated strain was observed using X-ray diffraction. I prepared the samples, participated in the experiment, and made minor contributions to the manuscript.

Paper V
This paper describes the study of nanowires using TXRD at the D611 beamline. The velocity of sound in the nanowires was measured. I was the person mainly responsible for the experiment, I carried out the data analysis, used the SEM and static X-ray diffraction to characterize the samples, and wrote the first draft of the manuscript.

Paper VI
This paper describes the study of nanowires using TXRD at the D611 beamline. The amount of light that gets absorbed in InSb nanowire has been studied. I was the person mainly responsible for the experiment, I carried out the data analysis, used the SEM and static X-ray diffraction to characterize the samples, and wrote the first draft of the manuscript.

Part II

Papers